NATURAL VARIABILITY IN THE EARTH'S CLIMATE SYSTEM

by

Jordan L. Thomas

A dissertation submitted to Johns Hopkins University in conformity
with the requirements for the degree of Doctor of Philosophy

Baltimore, MD

December 2017

Abstract

Lorem ipsum dolor sit amet, consectetur adipiscing elit. Donec malesuada turpis lorem, a malesuada nulla mollis non. Cras et enim id dui viverra pharetra nec a orci. Aenean malesuada mi arcu, vel mollis diam bibendum ac. Duis lorem quam, euismod id tellus ac, consequat tempor eros. Morbi tempor eu lacus non feugiat. In vel feugiat urna. Curabitur faucibus metus ac fringilla convallis. Aliquam non aliquet dui. Morbi sed nunc ut sem egestas malesuada.

Nulla condimentum dictum nisl sed sollicitudin. Morbi fermentum lobortis congue. Suspendisse lobortis dui eget nunc dictum maximus. Vestibulum ullamcorper leo nec sagittis iaculis. Duis diam dolor, facilisis sit amet vulputate pellentesque, tempus et sem. Pellentesque in ipsum ut metus ullamcorper hendrerit. Phasellus quam turpis, tristique in dictum a, cursus vitae justo. Duis feugiat tincidunt justo, volutpat convallis ligula tristique id. Pellentesque quis nibh commodo, semper quam vel, ultrices neque. Nam auctor commodo ipsum dapibus scelerisque. Duis rhoncus eros at pretium convallis.

Morbi placerat fermentum ex a porttitor. Vivamus rhoncus massa vel ex laoreet tincidunt. Etiam sit amet leo iaculis, posuere lacus ac, pretium felis. Aenean nisl leo, condimentum eu placerat ullamcorper, mollis quis neque. In ut porttitor quam. Pellentesque ac sapien in lorem posuere convallis. Suspendisse efficitur massa ac mollis luctus. Aliquam a pharetra purus. Mauris quam sem, scelerisque maximus urna non, imperdiet dictum enim. Vestibulum quis fringilla metus.

Etiam tempus odio in magna placerat maximus. Pellentesque efficitur, orci eu vulputate auctor, neque metus suscipit libero, id consequat ante ante sit amet

diam. Donec ut posuere elit, nec feugiat orci. Mauris at ipsum et quam finibus dictum vel et lorem. Aliquam et nulla dignissim, egestas orci vel, pellentesque purus. Suspendisse a libero vitae libero accumsan viverra vulputate nec nunc. Proin ultrices nulla eget accumsan efficitur. Duis vel sem luctus, vulputate risus sit amet, pretium tortor. Etiam eleifend.

Faculty Advisor and First Reader: Professor Darryn Waugh

Earth and Planetary Science Department, Johns Hopkins University

Second Reader: Professor Anand Gnanadesikan

Earth and Planetary Science Department, Johns Hopkins University

Acknowledgements

Lorem ipsum dolor sit amet, consectetur adipiscing elit. Ut posuere vehicula ligula a aliquet. Fusce imperdiet augue sapien. Suspendisse consequat ipsum a pulvinar bibendum. Morbi tincidunt non lorem mollis euismod. Nulla sit amet leo elementum, venenatis mi vel, finibus turpis. Curabitur fermentum tellus porta orci commodo, id cursus elit bibendum. Sed venenatis lacus nec malesuada posuere. Fusce at libero quis orci faucibus malesuada vitae quis nibh. Nunc sem odio, faucibus vel mauris id, ultricies luctus augue. Sed venenatis arcu eu augue luctus fringilla. Curabitur tincidunt metus et tellus eleifend, et consequat massa accumsan. Integer rutrum ullamcorper dignissim. Aenean cursus consectetur bibendum. Nulla et eros eu sapien tincidunt dapibus non vel tortor.

Curabitur tincidunt risus ut nibh sollicitudin, id luctus nunc imperdiet. Morbi ultrices viverra ex non facilisis. Integer ac auctor neque. Proin nisl leo, aliquet sed augue a, sollicitudin placerat dolor. Fusce ac auctor sapien, id pellentesque justo. Vestibulum faucibus.

Contents

List of Tables

List of Figures

CHAPTER 1

Introduction

1.1 Overview and aims

An introduction goes here

Recent trends and natural variability

Much of the work contained in this chapter is based upon *Thomas et al.* [2015], published in *Geophysical Research Letters*.

2.1 Overview and aims

The Southern Ocean plays a critical role in the ocean overturning circulation and moderating global climate through carbon and heat uptake [*Khatiwala et al.*, 2009; *Gnanadesikan*, 1999], with approximately 40% of anthropogenic carbon and 75% of heat entering the ocean south of 30°S [*Frölicher et al.*, 2014a; *Sabine et al.*, 2004]. The leading mode of Southern Hemisphere (SH) extratropical variability, the Southern Annular Mode (SAM), has been shown to directly affect this overturning circulation and the distribution of anthropogenic carbon uptake by altering the magnitude and location of the westerly jet [*Hall and Visbeck*, 2002; *Mignone et al.*, 2006; *Sen Gupta and England*, 2006]. It is therefore important to understand the variability in the SH extratropical circulation.

Observations and reanalyses have shown a positive trend in SAM and jet magnitude over the last couple decades along with a poleward shift in the jet location [*Thompson*

et al., 2000; *Thompson*, 2002] in addition to trends in subtropical sea surface temperature, Antarctic sea ice extent, ocean ventilation and gyre circulation [*Parkinson and Cavalieri*, 2012; *Swart and Fyfe*, 2012; *Waugh et al.*, 2013; *Roemmich et al.*, 2007]. Additionally, studies have detected anthropogenic influences in surface pressure and the westerly jet [*Gillett and Thompson*, 2003; *Gillett*, 2005]. These trends in the SAM and consequently the jet have been largely attributed to ozone depletion in the SH stratosphere during austral summer [*Previdi and Polvani*, 2014; *Gillett et al.*, 2013, 2003]. However, there is also evidence that this positive phase trend in the SAM is due in part to greenhouse gas warming [*Arblaster and Meehl*, 2006; *Lee and Feldstein*, 2013; *Gillett et al.*, 2013].

While there is evidence of anthropogenic forcing, understanding the forcing in the context of natural variability is difficult given the lack of in-situ observations and satellite information prior to 1979. Previous studies have tried to quantify the natural variability in the SH using proxy records [*Marshall*, 2003; *Visbeck*, 2009] and climate models [*Latif et al.*, 2013]. Understanding the relative contribution of natural variability and anthropogenic forcing to recent trends is critical to understanding how global climate will be influenced in the future.

In this study, we aim to further estimate the natural variability of the SH extratropical circulation by using the Coupled Model Intercomparison Project Phase 5 (CMIP5) pre-industrial control model runs. We examine five metrics of the SH extratropical circulation: the SAM, the jet location defined using the 850mb winds (U_{lat}) and the surface wind-stress (τ_{lat}), the jet magnitude defined by the 850mb winds (U_{max}) and the surface wind-stress (τ_{max}). We turn to CMIP5 pre-industrial model runs to quantify the natural variability of these five metrics to address the following questions: Can recently observed trends in SH circulation occur in CMIP5 piControl model runs due to natural variability alone, do the CMIP5 models historical (1980-2004) runs show significant trends in the circulation metrics, and do these simulated historical trends capture the characteristics of the observed trends?

2.2 Methods

In order to examine the natural multi-decadal-scale variability in the SH circulation we use a combination of pre-industrial control ("piControl") and historical (1980 to 2004) runs from models. Table 1 lists the models used in this study, the length of their piControl run and the number of historical runs. The models were chosen based on the availability of monthly-mean fields of sea level pressure, 850mb zonal winds and zonal wind-stress for both piControl and historical runs. We focused on the austral summer (averaged over December, January and February) because this is the season where the largest trends are observed [*Thompson*, 2002; *Thompson et al.*, 2011].

From the monthly sea-level pressure, we calculated the SAM as the zonal sea level pressure difference between 65º and 40º degrees South. For the sake of comparisons across different models, we chose to leave the SAM as a surface pressure difference as opposed to normalizing by the standard deviation as done in *Gong and Wang* [1999] to avoid normalizing by different standard deviations across models. Additionally, we examine the SH westerly jet magnitude and location calculated using both zonal surface wind-stress (τ_{max} and τ_{lat}) and 850mb zonal winds (U_{max} and U_{lat}). To find the jet maximum and location, the maximum zonal-mean wind-stress/850mb winds and the surrounding 4 grid-points were isolated and interpolated to a 0.1-degree meridional grid. A quadratic polynomial was then fit to the interpolated data and the maximum magnitude and location was found.

While there are no trends (i.e., drift) in these metrics over the length of the piControl time-series (order 250-1000 years), strong multi-decadal trends are found. Time-series in SAM from a high-varying model (MPI ESM MR) and a low-varying model (MIROC5) are shown in Figure 2.1a and c respectively. As highlighted in red, there are multiple 25-year periods that have strong trends even though there is no trend over the entire time-series. In order to quantify the variability of these multi-decadal-scale trends, we

Table 2.1: CMIP 5 models used in this study.

Model	piControl model run length (years)	Historical model ensemble runs
CanESM2	996	1
CNRM CM5	850	10
GFDL ESM2M	500	1
IPSL CM5a LR	1000	6
IPSL CM5a MR	300	3
IPSL CM5b LR	300	1
MIROC ESM	531	3
MIROC ESM CHEM	255	1
MIROC5	200	5
MPI ESM LR	1000	3
MPI ESM MR	1000	3
MRI CGCM3	500	3
NOR ESM1m M	501	1
NOR ESM1m ME	252	1

calculate the linear trend of each metric (SAM, τ_{max}, τ_{lat}, U_{max}, and U_{lat}) for consecutive and overlapping 25-yr trends for each model's piControl run (*Polvani and Smith* [2013] performed a similar analysis for sea ice extent in piControl runs).

We focus on the period 1980-2004 because reanalyses are unreliable before the implementation of satellites in 1979 (*Swart and Fyfe* [2012] Figure 1). Our analysis goes up until 2004 in order to compare with the CMIP5 historical model runs, which are typically run until year 2005. To verify that period length does not influence our results, the same analysis with CMIP5 piControl model runs and observations for the 34-year period between 1980-2014 was conducted (not shown). The results are essentially identical to those reported below as the observed changes over this period are either the same size or smaller than over the 1980-2005 period and the modeled trends are only slightly smaller.

The distribution of these 25-yr trends for the model piControl run is a measure of the natural multi-decadal variability in each model (in other words, the model internal variability with no anthropogenic influences). As an example, the probability density function (PDF) of these 25-year linear trends for the MPI ESM MR and MIROC5 models are shown in Figure 1b and d. The blue curve shows the probability density of the 25-
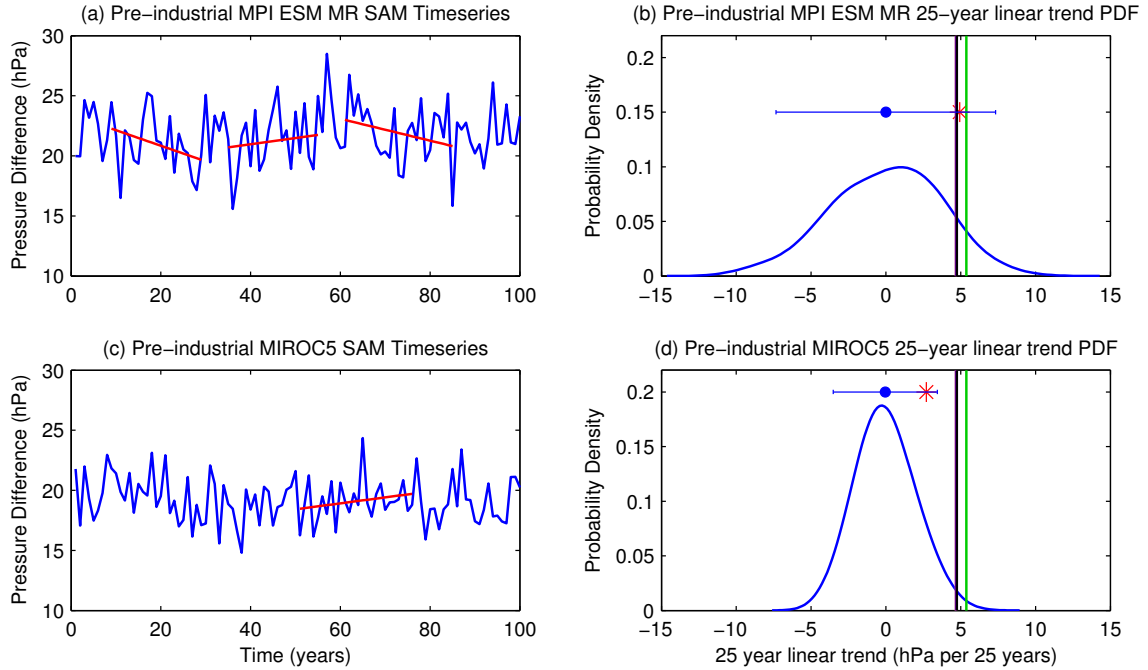
Figure 2.1: SAM time-series for (a) MPI ESM MR and (c) MIROC5 piControl runs over the first 100 years. The red lines indicate periods where the trend is greater than the average reanalysis trend between 1980-2004. Figures b and d show the probability density functions for the 25-year linear SAM trends in MPI ESM MR and MIROC5 respectively. The blue dot represents the mean of the 25-year trends while the whiskers extend 2 standard deviations. The vertical lines represent the observed trends: NCEP R1 (green), NCEP R2, ERA-Int, and JRA-55 (black), and the red asterisk shows the magnitude of the historical model run trend (first ensemble member).

year linear trends for the SAM, and the whisker plot shows the mean (blue circle) and 2 standard deviations (whisker extent) of the 25-year trends. The means of the 25-year trends (blue dot) are near zero, consistent with there being no drift in the piControl runs, but the trend for any individual 25-year period varies from -10 to +10 hPa per 25 yrs (with standard deviation of around 4 hPa per 25 yrs). Throughout the rest of the paper we shall use the whiskers to represent the distribution of 25-year trends from the model piControl runs. Each CMIP5 model has a different piControl run length, which could potentially impact our model-model comparisons. However, subsampling the output from 1000 year piControl runs shows limited sensitivity of the standard deviation of 25-yr trends for run lengths between 250 and 1000 yrs.

To compare the observations with the modeled natural variability, we used four re-

analysis products: NCEP Reanalysis 1 (NCEP-1) [*Kalnay et al.*, 1996], NCEP Reanalysis 2 (NCEP-2) [*Kanamitsu et al.*, 2010], ERA-Interim [*Dee et al.*, 2011], and JRA-55 [*Kobayashi et al.*] during the period 1980-2004. We also calculated the linear trend between the years 1980-2004 from the model historical runs, and compared both with the observed trends and model natural decadal variability. The vertical lines in Figure 1b and d represent the 1980-2004 reanalysis trends and the red asterisk shows historical simulation trend.

2.3 Results & Discussion

2.3.1 Natural Variability

We first examine the distribution of 25-year linear trends from CMIP5 piControl runs. Figure 2 shows, as whisker plots, the distributions of 25-year linear trends of (a) SAM, (b) U_{lat}, (c) τ_{lat}, (d) U_{max}, and (e) τ_{max}, for each model . For all five metrics, the mean 25-year linear trend (blue circles) is around zero for all the models, as expected for unforced model runs with no drift. The width of the whiskers is, however, variable across the different models, indicating differences in the multi-decadal variability among the models. Models with larger whiskers are more variable with stronger multi-decadal trends than models with smaller whiskers.

The variability of the whisker width among the models differs among the five metrics. The SAM (Figure 2a) shows the most variability among the models, with the width of the whiskers ranging from 3 hPa per 25 years to 10 hPa per 25 years (the mean and 2 sigma of the whisker length for the ensemble of models is 6 ± 3 hPa per 25 years). This indicates there is little agreement in the magnitude of the natural variability of the unforced system in SAM among the CMIP5 models. The jet location variability, U_{lat} (Figure 2b) and τ_{lat} (Figure 2c) also differs across the various models, but the differences are not as pronounced as in the SAM (whisker width is 2 ± 0.75 degrees per 25 years). There is even less variability between the models in jet magnitude. For the 850mb winds (Figure

Table 2.2: Probability of obtaining averaged reanalysis trend by only natural variability (first three columns) and natural variability + historical multi-model ensemble trend (second three columns).

Model	Natural Variability			Nat. Variability + Hist. Ensemble		
	SAM	U_{loc}	U_{max}	SAM	U_{loc}	U_{max}
CanESM2	**5.98**%	0.09%	0.03%	**35.4**%	**9.77**%	1.77 %
CNRM CM5	4.18 %	0.21%	0.28%	**34.2**%	**6.45**%	**6.71** %
GFDL ESM2M	**5.41**%	1.05%	0.71%	**32.1**%	**7.32**%	**6.92** %
IPSL CM5a LR	**17.24**%	2.79%	0.31%	**39.5**%	**13.0**%	**5.54**%
IPSL CM5a MR	**9.29**%	1.84 %	0.30%	**33.0**%	**7.31**%	4.70%
IPSL CM5b LR	**16.3**%	3.70 %	1.49%	**39.8** %	**15.3**%	**9.56**%
MIROC ESM	**5.69**%	0.078%	0.032%	**37.8**%	3.80%	2.36 %
MIROC ESM CHEM	**10.24**%	0.52%	0.044%	**34.4**%	**7.27**%	1.78%
MIROC5	1.18%	0.005%	0.36%	**26.7**%	2.13%	3.65 %
MPI ESM LR	**8.40**%	1.70%	0.81%	**34.8** %	**10.4**%	**6.67**%
MPI ESM MR	**9.50**%	1.81%	0.71%	**40.3**%	**12.3**%	**7.61**%
MRI CGCM3	**5.14**%	0.27%	0.93%	**37.0**%	**7.24**%	**9.33**%
NOR ESM1m M	3.98 %	0.09 %	0.05%	**32.6**%	**5.30**%	1.70 %
NOR ESM1m ME	3.63%	0.09%	0.04%	**33.3**%	4.46%	2.98 %

*Bolded values indicate a probability of 5% or higher.

2d) the whisker extent is 0.75 ± 0.25 ms^{-1} per 25 years, while for magnitude of the surface wind-stress (Figure 2e) it is approximately 0.015 ± 0.005 Pa per 25 years.

To better understand how these metrics compare to each other, we compare the linear correlations of each of the jet metrics with the SAM (Figure 3). The highest correlations occur between the SAM and the jet latitude metrics, with average R^2 values of 0.7 for both τ_{lat} and U_{lat}. The correlations between the SAM and jet magnitude metrics are significantly lower with average R^2 values at 0.5, with the R^2 values for correlations of SAM with τ_{max} always being greater than that of SAM with U_{max}.

The comparison of magnitude of natural decadal variability of the different metrics and correlation between the metrics shows our first key result: The SAM, jet location and jet magnitude metrics are not interchangable.

2.3.2 *Observed trends*

With a description of the natural variability from the piControl run for each model, we now compare the observed reanalysis trends to the modeled natural variability to exam-

ine if the observed trend is forced or natural. In each panel in Figure 2.2, the dashed horizontal lines show the magnitude of the observed reanalysis trends. As expected from the above analysis there are differences among the different metrics.

The observed SAM trend observations lie just within the whiskers for most of the models, indicating the observed trends lie within the model natural variability. To quantify this further, the probability of each model randomly obtaining a trend with the magnitude of the average reanalysis SAM trend or larger is shown in table 2 (column 1). 10 of the 14 models have a probability of 5% or greater, and thus there is a significant (at the 5% level) probability of obtaining the observed 25-year trend in the piControl simulations by chance alone. In other words, the observed trend over the period 1980-2004 in the SAM lies just within the edge of natural variability as described by these models. This result also holds for the period 1980-2014 (not shown).

The observed τ_{lat} and U_{lat} trends are just outside the model's natural decadal variability (Figure 2b and c). If we calculate the probability of each model obtaining the observed average reanalysis U_{lat} trend (table 2, column 2), then we see that no models have a probability of 5% or greater; however, 6 of the 14 have greater than a 1% probability. Thus, there is not a significant (at the 5% level) probability of obtaining the observed trend using natural variability alone.

In contrast, the observed trends in τ_{max} and U_{max} are both outside the natural variability as described by the models (Figure 2d and e). The probability of obtaining the average reanalysis U_{max} trend in all but one of the piControl models is less than 1% (table 2, column 3) and therefore there is not a significant (at the 1% level) probability of the natural variability reproducing the observed trend. The probabilities of the piControl τ_{max} and τ_{lat} obtaining the observed trends are not shown in table 2, but are consistent with the U_{max} and U_{lat} probabilities.

The above shows that the observed trends in the SAM largely lie at the edge of natural

9
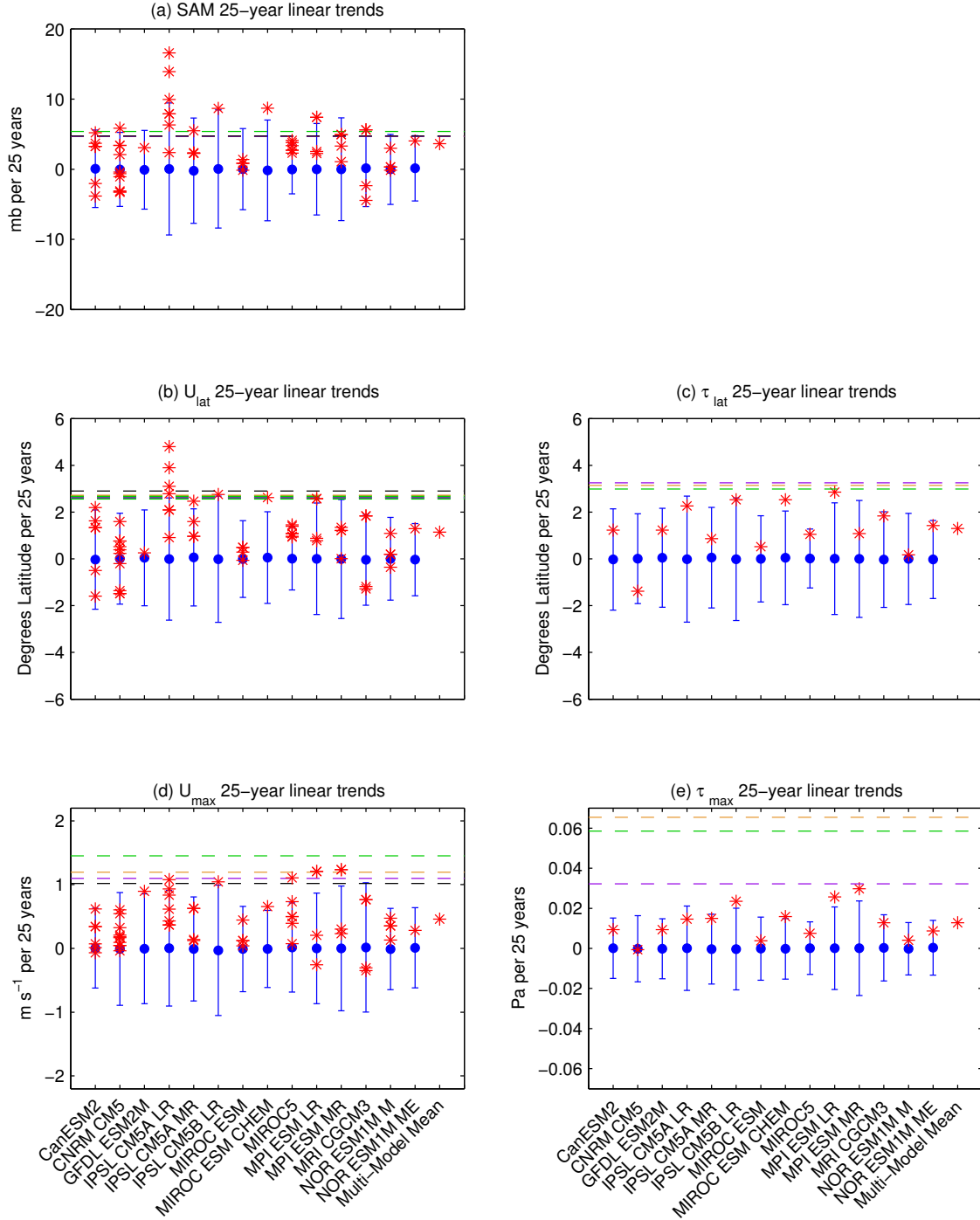
Figure 2.2: Natural variability, historical trends and observations for (a) SAM, (b) 850mb jet latitude, (c) wind-stress jet latitude, (d) 850mb jet magnitude, and (e) wind-stress jet magnitude. Blue circles show the mean of the piControl 25-year linear trends indicating model drift. Whisker length is 2 standard deviations. Red points show the historical run trends for each ensemble member. Horizontal dashed lines indicate the absolute value of the observed trends: NCEP R1 (green), NCEP R2 (orange), ERA-Int (purple), and JRA-55 (black).

multi-decadal variability of the piControl model runs. However, this does not necessarily mean that the observed trends are not forced by anthropogenic activities, merely that the observations can contain a large component of natural variability in the SAM. The observed trend in the jet location and magnitude, however, is outside the variability of most models piControl runs. This does suggest an external force driving the jet to strengthen and shift over this 25-year period.

2.3.3 *Model historical trends*

We now examine the model historical runs to understand how the modeled trends compare to the modeled natural variability and to compare the modeled trends with the observed trends. The red asterisks in Figure 2 represent the 25-year trend for each historical run (the number of historical runs varies among the models).

There is considerable variability amongst the models in the magnitude of the trends, but for all five metrics the vast majority of the simulated historical trends are of the same sign (increase in SAM, poleward shift and strengthening of the jet). This consistency in sign indicates that external (anthropogenic) forcing is causing at least part of the trend. However, the magnitude of the historical trends are almost all within the natural multi-decadal variability of the corresponding model (i.e. within the whiskers). Thus while the response in the models between 1980 and 2004 is due (at least in part) to forcing, the response does not overwhelm the natural variability.

For the SAM, the magnitude of the individual historical ensemble member trends are largely within the estimated natural variability and highly variable, with some ensemble members having trends of the opposite sign to the observations (dashed horizontal lines). Because the observed trends are generally within the natural decadal variability of the models a close agreement between individual historical ensemble members and observed trends would not be expected due to the high component of natural variability. Most

of the ensemble members have positive trends and the magnitude of the multi-model ensemble mean historical trend is similar to the observations. This further suggests an anthropogenic forcing pushing the SAM towards positive phase.

The same comparison for jet location and magnitude yields different results. The observed trends in the jet metrics are outside the natural variability of the models, and generally larger than the modeled historical trends (especially for the magnitude of the wind stress). A possible cause for this is that the observed trends are due to anthropogenic forcing that is not well represented (or under represented) in the models. However, another possibility is that there are issues with the reanalyses and the reanalyses are overestimating the real trend. This may especially be the case for the NCEP reanalyses, where the wind stress trends are significantly outside the model natural variability but the 850 hPa winds are just outside the model natural variability.

If we consider the observed trends to be a combination of natural variability and external forcing, and if we use the ensemble-mean historical trend as a representation of the forced response, we can better capture the observed trend. The last 3 columns in table 2 show the probability of obtaining the mean reanalysis trend from a combination of each model's natural variability and the multi-model ensemble mean historical trend (results for τ_{lat} and τ_{max} are not shown, but are consistent with U_{lat} and U_{max}). The probabilities for each metric are substantially greater, indicating that there is a significant probability, in most models, that the observed trends are due to this combination of natural variability and anthropogenic forcing. This does not exclude the possibility that the models are systematically biased low, or that the reanalyses are biased high, but it suggests that the mismatch is smaller than might be suggested from previous work [*Swart and Fyfe*, 2012].
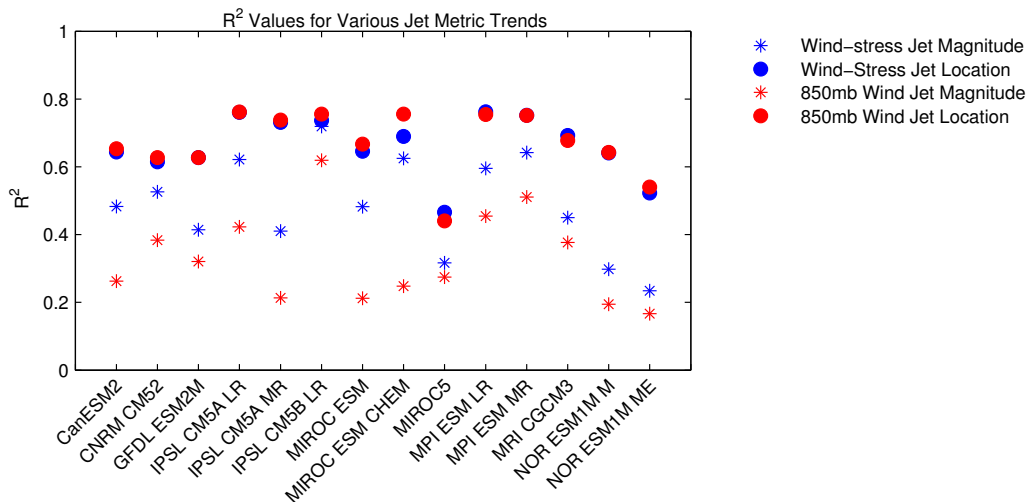
FIGURE 2.3: Correlation coefficient squared for correlation of the the 25-year linear trends in wind-stress jet location, wind-stress jet magnitude, 850mb jet location, and 850mb jet magnitude with the 25-year trends in SAM for each model.

2.4   Conclusions

Changes in the SAM are often linked with concurrent changes in the SH westerly jet magnitude and location [*Hall & Visbeck*, 2002]. Additionally, observational studies have shown recent trends in these diagnostics and attribute them to a combination of ozone depletion and greenhouse gas induced warming [*Arblaster and Meehl*, 2006]. By comparing CMIP5 models piControl and historical runs with reanalysis observations, we have shown that there are significant differences in the observed and modeled trends of the SAM from those in the jet. Hence, the SAM and jet metrics cannot be used interchangeably.

Examining the natural variability of the SAM using CMIP5 preindustrial control runs has led to the conclusion that the observed trend is not decisively outside the natural variability as simulated by the CMIP5 models. While the modeled natural variability in SAM in quite large, the positive bias of the model historical trends suggest influence of an external forcing. The failure of individual historical models to simulate the magnitude of the observed historical trend could be due to the natural variability and not deficiencies in the simulations.

In contrast, the observed trends in jet location and magnitude are outside the natural variability of the models. The historical model runs also seem to underestimate the magnitude of these trends, especially in jet magnitude. Combining the natural variability and historical trend brings the models closer to capturing the observed trends in jet location and magnitude, but this does not eliminate the possibility that the model trends are biased low or the reanalyses are biased high.

Changes in the SAM and SH westerly jet have been linked with significant changes in ocean circulation, ocean heat and carbon uptake [*Mignone et al.*, 2006], and Antarctic sea-ice extent [*Fan et al.*, 2014]. We suggest that changes in SAM and jet latitude may behave differently than changes in jet magnitude and thus may have independent effects on the Southern Ocean and Antarctic climate. Understanding how these atmospheric variables interact with each other will be critical for predicting the future evolution of ocean circulation and the earth system.

CHAPTER 3

Ocean heat and carbon variability

Most of the work contained in this chapter is based upon *Thomas et al*, *2017*, submitted to in *Journal of Climate*.

3.1 Introduction

The global ocean is an important component of the climate system. Holding far more heat and carbon than the atmosphere, it is an important sink for anthropogenic carbon and heat generated from greenhouse gas emissions. Observational estimates suggest that as of 1995, the ocean has been responsible for the uptake of approximately 100 Pg of anthropogenic carbon [*Khatiwala et al.*, 2012; *Sabine et al.*, 2004; *Waugh et al.*, 2006]. Temperature observations have also been used to estimate that the upper 2000 m of the ocean has been a sink for 15×10^{22} J of excess heat [*Levitus et al.*, 2009] between the years 1975–2005. Additionally, *Frölicher et al.* [2014a] demonstrated that in climate model simulations the Southern Ocean is an important region for oceanic uptake of anthropogenic carbon and heat. They estimate that 30% of anthropogenic carbon and 75% of anthropogenic heat that enters the ocean does so south of 30°S.

However, changes in the circulation due to both anthropogenic forcing and natural variability may play an important role in heat and carbon uptake. Many studies have examined how changes in Southern Ocean circulation impact ocean carbon content [*Sarmiento and Toggweiler*, 1984; *Sarmiento and Le Quere*, 1996; *Marinov et al.*, 2008]. Between the 1980's to early 2000's, multiple studies linked an acceleration of the wind-driven Southern Ocean overturning with the resulting increase in upwelling of carbon-rich waters resulting in a decrease in the Southern Ocean CO_2 sink despite an increase in atmospheric CO_2 [*Le Quere et al.*, 2000; *Lovenduski et al.*, 2007; *Lenton et al.*, 2009]. More recently however, observational studies have suggested this weakening of the Southern Ocean carbon sink has reversed [*Landschutzer et al.*, 2015; *Devries et al.*, 2017], highlighting the importance of understanding natural variability. Finally, in many models, Weddell Sea deep convection has been determined to cause large fluctuations in ocean heat [*Latif et al.*, 2013; *de Lavergne et al.*, 2014] and carbon content [*Bernardello et al.*, 2014]. While significant effort has gone into understanding the net uptake of both heat and carbon, less research has focused on the natural fluctuations of heat and carbon content associated with longer (decadal-to-centennial) timescales of variability.

It is additionally important to examine heat and carbon variations together. A recent paper by *Winton et al.* [2013] showed that the impacts on heat and carbon uptake are different in response to changing ocean circulation. A change in ocean circulation has a larger influence on oceanic heat uptake than carbon uptake. This supports the results of *Banks and Gregory* [2006] and *Xie and Vallis* [2012] who show that temperature in the ocean does not in fact behave as a passive tracer.

While studies have focused on the forced response of oceanic heat and carbon and have demonstrated that heat and carbon have different storage and uptake patterns, we are unaware of any studies that have explored the un-forced co-variability of heat and carbon content. In this paper, we investigate natural variability of both heat and carbon content in multiple simulations of an Earth-system model. We examine the magnitude

and frequency of the variability in global heat and carbon content in simulations with various mesoscale mixing parameter settings. We then look more closely at the regional and spatial patterns of variability and finally, we propose possible mechanisms that drive this variability. Varying the mesoscale mixing parameters allows us to test the sensitivity of the patterns of variability and the mechanisms driving this variability. This analysis aims to help understand the magnitude of natural variability and provide a context with which to view anthropogenic trends. Additionally it aids in the understanding of how carbon and heat vary with respect to each other.

Descriptions of the model used and quantities examined is found in section 4.2. Section 3.3 discusses the temporal and spatial variability in heat and carbon content. The mechanisms driving this variability are examined in section 3.4, and conclusions are in section 3.5.

3.2 Methods

3.2.1 *Model and Simulation Descriptions*

We use the GFDL ESM2Mc [*Galbraith et al.*, 2011], a coarse resolution configuration of the GFDL ESM2M [*Dunne et al.*, 2012]. The model has an atmospheric resolution of 3.875°× 3° with 24 vertical levels. The ocean model is non-Boussinesq, using pressure as the vertical coordinate, and has a resolution of 3°× 1.5° and 28 vertical levels. Despite its relatively coarse resolution, ESM2Mc has a realistic simulation of the Southern Annular Mode [*Galbraith et al.*, 2011], response of Southern Hemisphere winds to an ozone hole [*Seviour et al.*, 2017], and El Niño Southern Oscillation [*Russell and Gnanadesikan*, 2014]. The vertical tracer diffusion coefficient (K_v) value is set within the KPP module. The value increases with depth and buoyancy forcing. When the water column is statically unstable the value can exceed 4 m s^{-2} which implies an equilibration time of approximately 5 days even for a water column that is 4000 m deep. The oceanic model also has a coupled biogeochemical

module referred to as the Biogeochemistry with Light Iron Nutrients and Gases (BLING) model [*Galbraith et al.*, 2010]. Although this module uses a highly parameterized biological cycle, it predicts patterns of carbon and oxygen change in response to global warming that are very similar to a more complex biogeochemistry simulation in ESM2M [*Galbraith et al.*, 2015].

Because of the coarse resolution, processes associated with oceanic eddies are parameterized. The mesoscale advection of tracers along isopycnals is parameterized using the Gent-McWilliams parameterization scheme [*Gent and Mcwilliams*, 2010]. The diffusion coefficient, A_{GM}, varies spatially depending on the meridional gradient of the vertical shear between 100 m – 2000 m. A default minimum and maximum value of A_{GM} is imposed at 200 m^{2}s^{-1} and 1400 m^{2}s^{-1} respectively. Additionally, the along-isopycnal diffusion (neutral diffusion) by mesoscale eddies is parameterized using a coordinate rotation method [*Redi*, 1982]. The neutral diffusion coefficient, A_{redi}, is set to a spatially constant value of 800 m^{2}s^{-1} by default.

The model was initialized using the World Ocean Atlas present-day observations of temperature, salinity, and nutrients and was run for 1500 years with pre-industrial (1860) values of greenhouse gases and aerosols. An additional 500 years were simulated using the default value of A_{redi} (800 m^{2}s^{-1}) and this simulation is referenced as the *control* simulation. At year 1500, the model was branched to produce two more 500-year simulations using different, constant values of A_{redi} = 400 and 2400 m^{2}s^{-1}. These runs are referred to as the *low eddy diffusion* and *high eddy diffusion* runs respectively. As discussed in *Pradal and Gnanadesikan* [2014] and *Gnanadesikan et al.* [2015], the value of A_{redi} varies significantly across modern climate models, which tend to use values lower than observational estimates [*Ollitrault and Colin de Verdière*, 2002]. The range of values used here is comparable to those seen in the CMIP5 model suite. One final 500-year simulation was conducted by branching the control run and changing the minimum value of the mesoscale eddy advection coefficient, A_{GM}, to be 600 m^{2}s^{-1} while maintaining the default value of A_{redi}

($800\,\mathrm{m^2s^{-1}}$). This is referred to at the *high eddy advection* simulation.

Figure 3.1 shows the winter-time climatologies (JJA) for various Southern Hemisphere metrics with comparison to observations for all simulations. The Southern Ocean temperature (Figure 3.1 (a)) in the surface layer is biased warm for all simulations. Additionally, all simulations except the *high eddy diffusion* simulation have subsurface temperatures exceeding the observations. Similarly, the modeled surface salinity (Figure 3.1 (b)) is biased fresh for all simulations except the *high eddy diffusion* simulation. Figure 3.1 (c) shows the profile of density stratification strength ($\sigma_0 - \sigma_0^{1500\mathrm{m}}$). The model simulations envelop the observational density stratification with the *high eddy advection* simulation having the strongest density stratification and the *high eddy diffusion* simulation having the weakest stratification. The comparison of the modeled Southern Hemisphere westerly wind stress with the ERA-Interim westerly wind stress is shown in Figure 3.1 (d). All the model simulations underestimate the strength of the wind stress south of 40°S and have an equatorward-biased peak in the wind stress. Finally comparison with the observational sea ice-extent is shown in Figure 3.1 (e). All simulations under estimate the sea ice extent in all months except the *high eddy advection* simulation which has accurate sea ice extent values in the austral spring.

The various A_redi simulations are discussed at length in *Pradal and Gnanadesikan* [2014] and *Gnanadesikan et al.* [2015], which examine the mean climate response and sensitivity of anthropogenic carbon uptake to changing the A_redi parameter. Here instead, we use the various simulations to test the robustness of the mechanisms driving the co-variability of heat and carbon. Because the different simulations have varying Weddell Sea convective variability (similar to the spread in CMIP5 models, see below), we can see if convection alters the mechanisms driving the co-variability of heat and carbon in this model. Unlike the CMIP5 suite where differences in biological models, atmospheric radiation code, and sea ice formation contribute to intermodel spread, our simulations differ only in the mesoscale parameterizations to isolate the influence of Weddell Sea convection
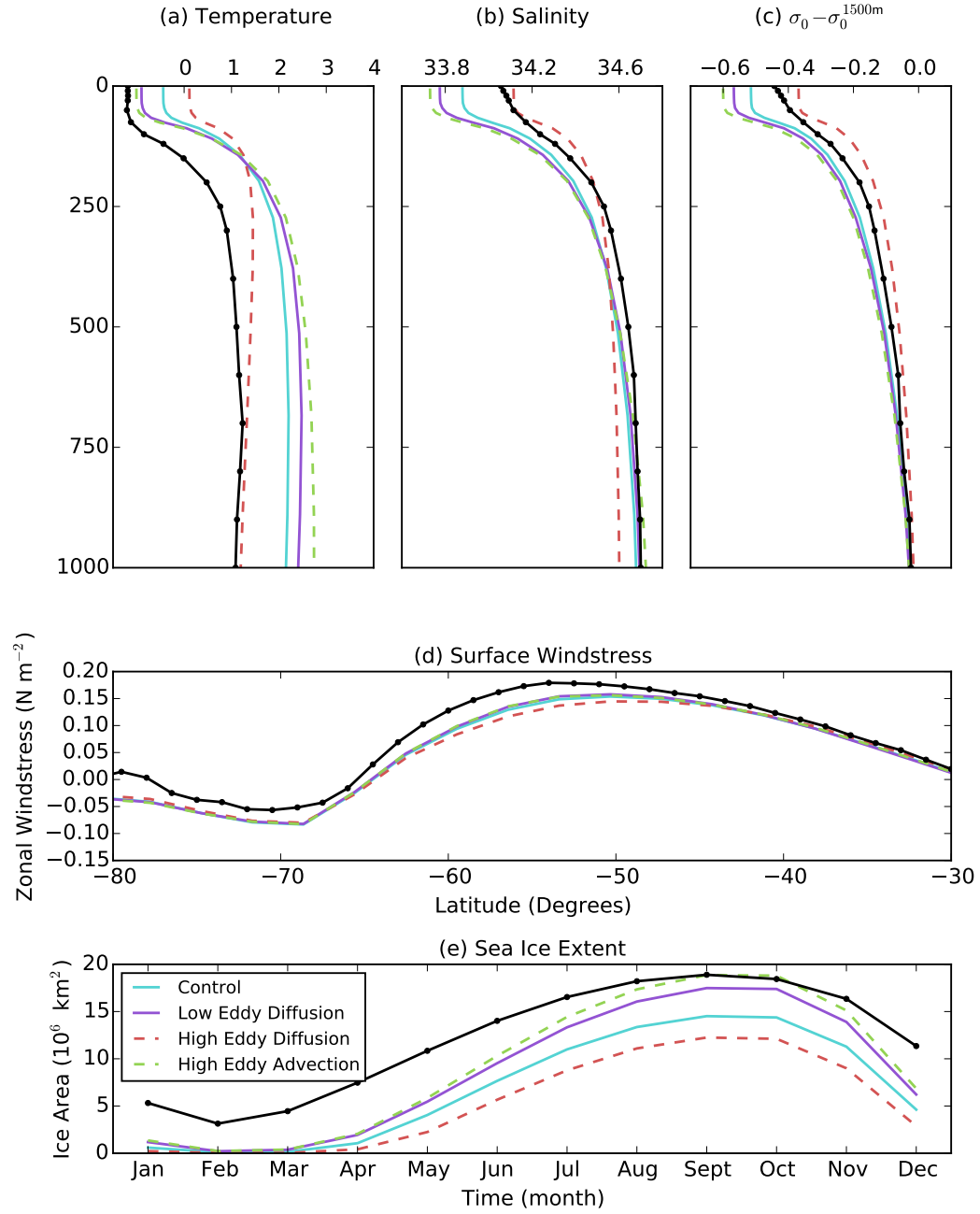
Figure 3.1: Comparison of control (blue), low eddy diffusion (purple), high eddy diffusion (red), and high eddy advection (green) simulations. JJA Southern Ocean (60–90°S) (a) temperature (b) salinity and (c) density stratification ($\sigma_0 - \sigma_0^{1500m}$). (d) JJA zonal surface wind stress and (e) Antarctic sea ice extent. Observational data for each metric is shown in black. Temperature, salinity, density stratification are estimates from the 2001 World Ocean Atlas 2001 dataset [*Boyer et al.*, 2002]. Surface wind stress are from ERA-Interim and averaged between 1979–2015. Sea extent is calculated using the National Snow and Ice Data Center Sea Ice Index [*Fetterer et al.*, 2016]

on the co-variability of heat and carbon content.

3.2.2 Heat and Carbon Content

Heat and carbon content are calculated globally and regionally. The oceanic heat content (H) is calculated using the subsurface potential temperature (θ), and integrated globally:

$$H_{global} = \sum_{k=0}^{bottom} \sum_{j=-90}^{90} \sum_{i=0}^{360} \rho c_p \theta \delta x_i \delta y_j \delta z_k \qquad (3.1)$$

Similarly, carbon content is calculated using Dissolved Inorganic Carbon (DIC) concentration and integrated globally:

$$C_{global} = \sum_{k=0}^{bottom} \sum_{j=-90}^{90} \sum_{i=0}^{360} \rho [DIC] \delta x_i \delta y_j \delta z_k \qquad (3.2)$$

Because the oceanic heat and carbon reservoirs are so large ($150,000 \times 10^{22}$ J and $37,000$ PgC, respectively), and the natural variability relatively small ($\pm 3 \times 10^{22}$ J and ± 3 PgC, respectively), we express the variability as an anomaly from the climatological mean.

3.2.3 Surface Heat Flux

We determine the surface heat flux by vertically integrating the vertical diffusion term over the entire water column and subtracting the geothermal heat flux from the sea floor:

$$\sum_{k=0}^{bottom} \left(\rho_k c_p \left(\frac{\partial \theta}{\partial t} \right)_{vdiff} \right)_k \delta z_k - Q_{geo} = \qquad (3.3)$$
$$Q_{SW} + Q_{LW} + Q_{latent} + Q_{sensible} = Q_{surface}$$

The advantage to defining the surface heat flux with this method, as opposed to the model-calculated surface heat flux, is that we can determine the heat lost to overlying sea ice in addition to the atmosphere as well as track heat sinks such as the melting of snow.

(a) Carbon

(b) Heat
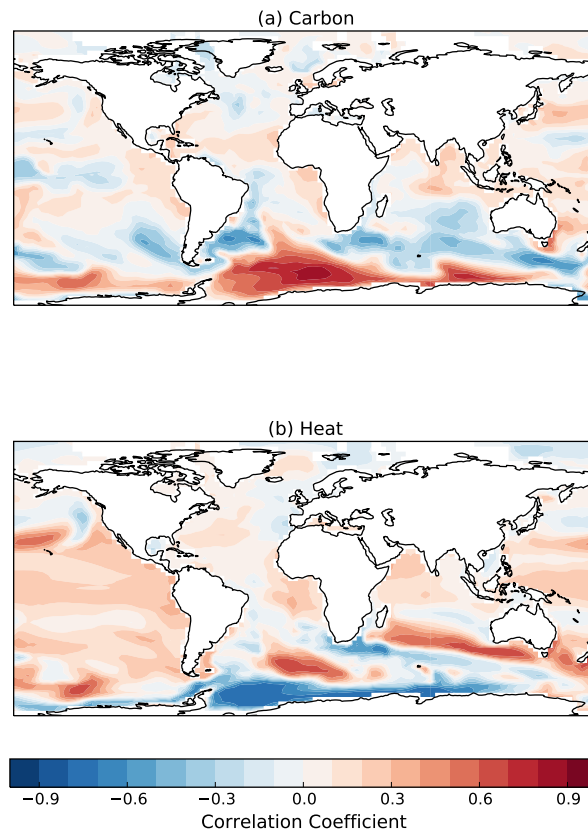
Figure 3.2: Correlation between (a) vertically integrated carbon content at each location and global carbon content and (b) vertically integrated heat content at each location and global heat content for the control simulation ($A_{redi} = 800$ m s^{-2}).

3.2.4   Southern Ocean

As has been previously documented [*de Lavergne et al.*, 2014], ESM2Mc has a particularly active Southern Ocean. Deep convective events occur often in the Southern Ocean, and have a sizable impact on the climate system. *Cabre et al.* [2017] recently showed that Southern Ocean convective events in this model have an impact on the Southern Hemisphere surface temperatures, Hadley cell, and radiative balance. In light of the Southern Ocean influence in this model, we first assessed the contribution of Southern Ocean variability to global heat and carbon variability. Figure 3.2 shows the correlation between vertically integrated carbon (heat) content at each location with the global carbon (heat) content in the *control* simulation. This initial analysis suggests the importance of the Southern Ocean, and particularly the Weddell Sea on global heat and carbon variability and will be more thoroughly examined in section 3.3.

3.3   Temporal and Spatial Variations in Heat and Carbon Content

3.3.1   Weddell Sea Convection

In the mid-1970s, an anomalous opening in the sea ice in the Weddell Sea was observed [*Carsey*, 1980]. Named the Weddell Polynya, this large opening was observed for three consecutive austral winters: 1974–1976. The polynya was formed and maintained by vigorous convective mixing where the upward flux of deep and relatively warm waters provided enough energy to melt the above sea ice [*Gordon*, 1982; *Martinson et al.*, 1981]. This heat loss at the surface resulted in subsurface cooling deep into the water column, depleting the subsurface heat reservoir.

While a large feature like the Weddell Polynya has not been observed since and is considered to be a rare event, these polynya events can be quite common in climate models. A recent paper by *de Lavergne et al.* [2014] quantifies these convective events in CMIP5 model preindustrial control simulations and shows the spread across models. They find

that some CMIP5 models have very little convection, while others have constant deep convection, with most models lying somewhere in between.

Changing the mesoscale eddy parameterization in our model suite has a large impact on the Weddell Sea deep convection. Figure 3.3 shows the annually-averaged subsurface temperature as a function of time (colored contours) and the annual mixed layer depth (black line) averaged over the Weddell Sea (60–80°S, 60°W–0). The downward spikes in mixed layer depth, and the concurrent decline in subsurface temperature indicate the occurrence of a deep convective event. The simulations range from no convection in the *high eddy advection simulation* (Figure 3.3 (d)), to constantly convecting in the *high eddy diffusion simulation* (Figure 3.3 (c)), with the *control* and *low eddy diffusion* cases oscillating between convective and non-convective periods (Figure 3.3 (a) and (b)).

When the neutral diffusion coefficient (A_{redi}) is increased as in the *high eddy diffusion* simulation, the along isopycnal diffusive mixing is increased. In the Southern Ocean where the isopycnals slope up to the surface and the subsurface water is warmer than the surface ocean, this increased along-isopycnal diffusion acts to decrease the vertical gradient in temperature and salinity (also shown in Figure 3.1 (a) - (c)). This results in a lower subsurface temperature, a weaker density contrast between deep and surface waters, less subsurface heat build-up, and no large convective 'events' (Figure 3.3 (c)). Alternatively, a lower neutral diffusion coefficient as in the *control* and *low eddy diffusion* simulations does the opposite: the along-isopycnal diffusive mixing is decreased and subsurface heat is able to build up until a deep convective event occurs (Figure 3.3 (a) and (b)).

Changing the eddy advection coefficient (A_{GM}) on the other hand impacts the slope of the isopycnal surfaces. As shown in *Gent et al.* [1995], increasing A_{GM} acts to flatten the isopycnal surfaces and reduce vertical exchange. In the Southern Ocean where the isopycnals slope up to the surface, and the A_{GM} value is usually small, increasing the minimum value of A_{GM} thus reinforces the vertical density gradient. The result is a build-up
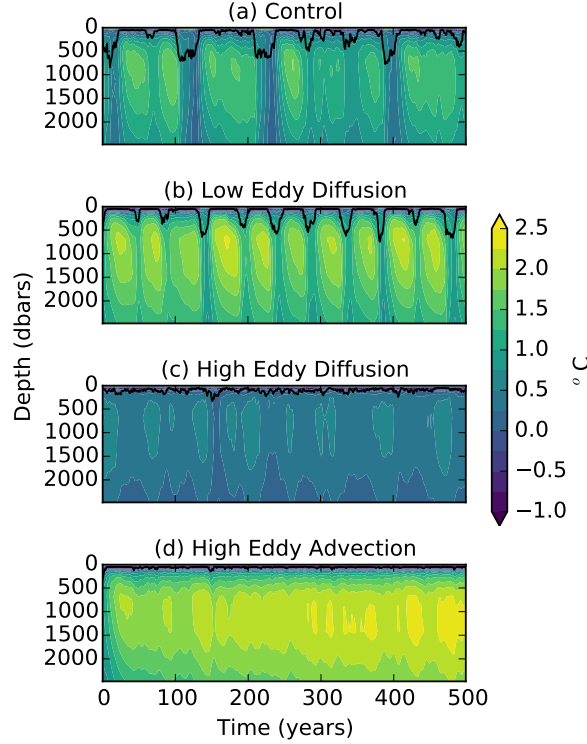
FIGURE 3.3: Annually averaged subsurface temperature (color contours) and mixed layer depth (solid black line) averaged over Weddell Sea for (a) Control simulation (A_{redi} = 800 m s^{-2}), (b) Low Eddy Diffusion simulation (A_{redi} = 400 m s^{-2}), (c) High Eddy Diffusion simulation (A_{redi} = 2400 m s^{-2}), and (d) High Eddy Advection simulation (GM_{min} = 600 m s^{-2}).

of subsurface heat that continues to grow throughout the *high eddy advection* simulation. The reinforced density gradient is strong enough to suppress deep convection throughout the 500-year simulation (Figure 3.3 (d)).

It is important to note that while the existence of subsurface heat build-up is known to be important for the existence of deep convective events, it is not yet known what mechanism initiates deep convection in the model or sets the timescales for convective variability. We have found, however, that by changing these parameterizations, we are able to span the range of convective variability seen in CMIP5 models as shown in *de Lavergne et al.* [2014] without the additional complications introduced by different representations of atmospheric processes and biological cycling. In this paper we will use these different convective states of the model to identify the impact convective variability has on both carbon and heat in the Southern Ocean and globally.

3.3.2 Global Heat and Carbon Variability

We first aim to understand the variability in global oceanic heat and carbon content in the *control* simulation. The time-series of global carbon and heat content anomaly is shown in Figure 3.4 (a) and (b). Both quantities show strong multi-decadal-scale variability, undergoing strong fluctuations roughly every 50 years. The magnitude of global carbon variability is about ± 3 PgC which accounts for only approximately 3% of the estimated anthropogenic uptake of carbon over the past few decades [*Khatiwala et al.*, 2012; *Sabine et al.*, 2004; *Waugh et al.*, 2006]. The variability in global heat content on the other hand is about ± 3 ×10^{22} J. This is a much larger percentage (20%) of the estimated uptake of anthropogenic in heat recent decades [*Levitus et al.*, 2009]. Figure 3.4 (c) shows the time-series of Weddell Sea (WS) subsurface temperature (averaged between 1500 m and 2500 m). This quantity has been shown to be a good proxy for WS deep convection since the subsurface temperature is significantly decreased during convective events [*Bernardello et al.*, 2014]. Comparing the time-series of the WS subsurface temperature to those of global heat and carbon anomalies, it is apparent that there is a strong relationship. In the control simulation, the WS subsurface temperature explains 61% and 35% (r^2) of the variance in global heat content and carbon content respectively (Table 3.1), with the strongest correlation occurring at time lag = 0. The correlation between WS subsurface temperature and global heat and carbon content is also high for the *low eddy diffusion* simulation, while the relationship is less strong (yet significant) for the *high eddy diffusion* and *high eddy advection* simulations (Table 3.1). These results suggest that WS convection is closely tied to the global heat and carbon content.

The global heat and carbon content anomaly time-series for all simulations is shown in Figure 3.5. The magnitude and frequency of heat and carbon content variability changes substantially across the different simulations. Comparing the time-series of global carbon content and heat content anomalies in the control simulation we find that they are anti-
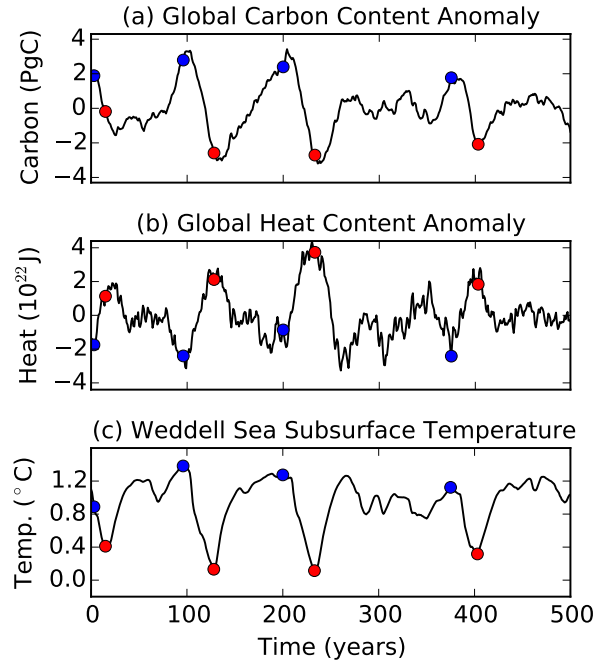
Figure 3.4: Carbon content anomaly, heat content anomaly and Weddell Sea subsurface temperature (averaged between 1500–2000 m, 0°–60°W, 60°–80°S) for control simulation. Blue circles indicate beginning of convection and red circles indicate end of convection defined using four strongest local maxima and minima in Weddell Sea Subsurface Temperature.

correlated ($r = -0.629$, Figure 3.6). Given that in this model, the global heat and carbon are primarily driven by Southern Ocean variability and Southern Ocean convection acts to deplete the Southern Ocean of both carbon and heat content, we would expect that global heat and carbon content should vary together. Therefore it is surprising that the two quantities are so strongly negatively correlated.

This anti-correlation relationship between global heat and carbon content is consistent in the additional simulations as well (Figure 3.5). Figure 3.6 shows the Pearson correlation coefficient between global heat and carbon content for each simulation. All of the simulations have a statistically significant negative correlation between global heat and carbon exceeding -0.3. The two simulations which oscillate between convective and non-convective periods (*control* and *low eddy diffusion*) have stronger correlations at or exceeding -0.5. The fact that significant anti-correlation is found for all simulations suggests that the mechanisms causing this anti-correlation in global heat and carbon content are

27
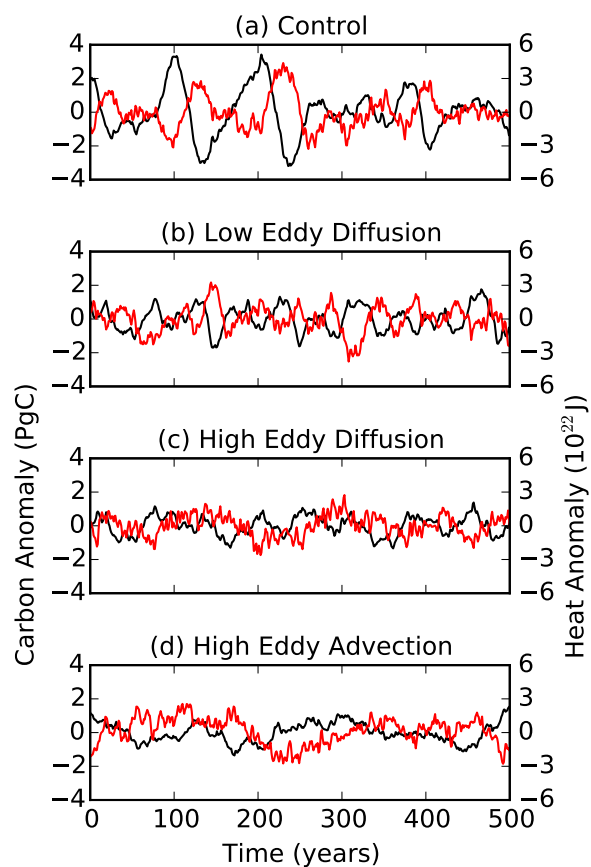
Figure 3.5: Globally integrated carbon content anomaly (black) and heat content anomaly (red) for (a) Control simulation (A_{redi} = 800 m s^{-2}), (b) Low Eddy Diffusion simulation (A_{redi} = 400 m s^{-2}), (c) High Eddy Diffusion simulation (A_{redi} = 2400 m s^{-2}), and (d) High Eddy Advection simulation (GM_{min} = 600 m s^{-2}).

Table 3.1: Relationship between Weddell Sea subsurface temperature and global carbon and heat content anomalies. All correlations are statistically significant from 0 (p = 0.005).

Simulation	Carbon Content	Heat Content
	Correlations (r)	
Control	0.59	-0.79
Low Aredi	0.61	-0.56
High Aredi	0.49	-0.20
High GM$_{min}$ min	0.12	-0.24

not strongly dependent on the convective state in the WS.

In light of these results, we find it helpful to divide these simulations up into two classes: the *low mixing simulations* which oscillate between convective and non-convective periods (control and low eddy diffusion) and the *high mixing simulations* simulations which do not (high eddy diffusion and high eddy advection). The low mixing simulations are characterized by a build-up and subsequent release of abyssal heat content in the Southern Ocean (Figure 3.3). These two simulations also have very strong oscillations in the global heat and carbon content, closely linked to the WS convection. The high mixing simulations on the other hand do not show this oscillation between subsurface build-up and release in the Southern Ocean, but rather either constant depletion in subsurface temperature in the *high eddy diffusion* (Figure 3.3 (c)) or a constant build-up of subsurface temperature in the *high eddy advection* (Figure 3.3 (d)). The lack of these oscillating convective states results in smaller global heat and carbon variability (Figure 3.5), and a weaker relationship (although significant) between the WS and the global heat and carbon content.

To understand why the global heat and carbon are strongly anti-correlated, next we look at the regional relationships between heat and carbon content.
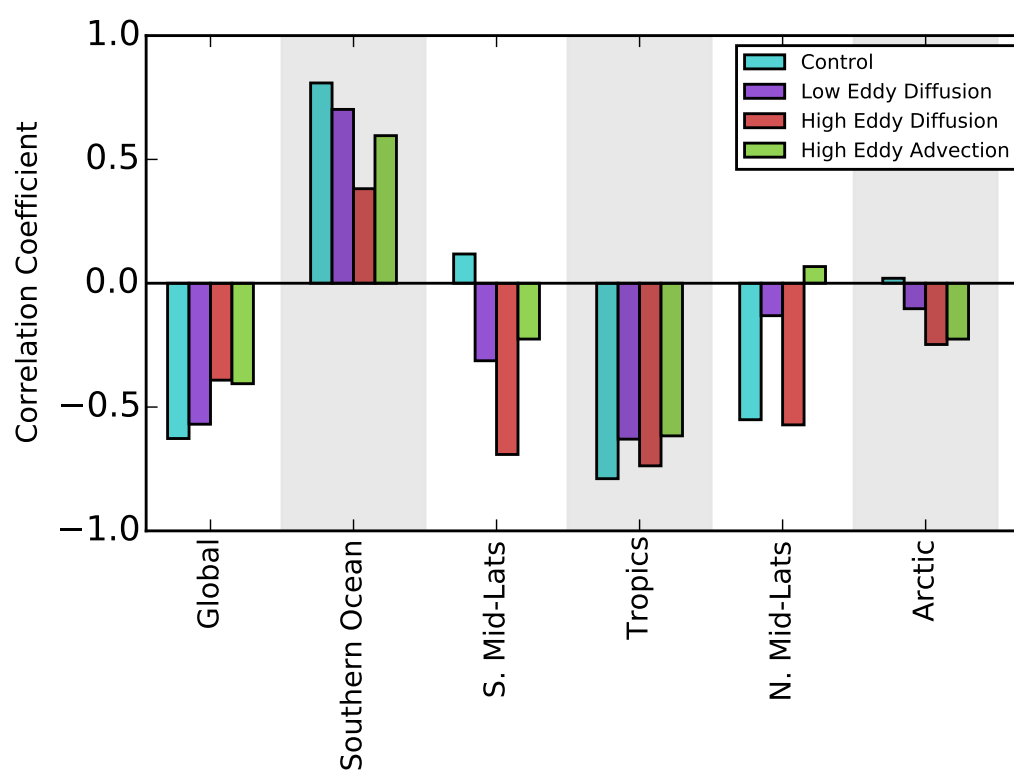
Figure 3.6: Pearson correlation coefficients for integrated carbon content anomaly versus integrated heat content anomaly for each region.

3.3.3   Regional Heat and Carbon Variability

To diagnose which regions significantly contribute to the observed variability in global heat and carbon content, we break the global ocean into zonal bands: the Southern Ocean (90^oS–55^oS), the southern mid-latitudes (55^oS– 20^oS), tropics (20^oS–20^oN), the northern mid-latitudes (20^oN– 60^oN), and the Arctic (60^oN–90^oN). These divisions were defined by the zonal average of the zero wind-stress curl in order to isolate the dynamical regions (not shown). The correlation coefficients between heat and carbon content in each of these regions are also shown in Figure 3.6. The correlation coefficients give a sense of what remains consistent across the simulations even with the different convective states. The Southern Ocean has a strong positive correlation between heat and carbon for all the simulations. Additionally, in the tropics there is a strong negative correlation between heat and carbon for all the simulations. This result suggests that the negative correlation in the tropics is key to understanding the negative correlation between heat and carbon seen globally.

To get a better sense of which regions dominate the variability, we decompose the global heat and carbon regionally by regressing the regional inventories of heat and carbon against the global inventories of heat and carbon. We first consider heat content in the *control* simulation (Figure 3.7 (a), red dots). The regression highlights the importance of three regions in contributing to the global heat content signal: the Southern Ocean, southern mid-latitudes, and tropics. The Southern Ocean regression coefficient has a magnitude similar to the southern mid-latitudes and tropics, but the opposite sign. This indicates that the variability in Southern Ocean heat content is being compensated by similar magnitude variability in heat content in both the southern mid-latitudes and tropics.

The picture is nearly identical in the *low eddy diffusion* simulation (which also undergoes oscillations between convective and non-convective states). The Southern Ocean heat content variability is compensated by similar magnitude variability in both the southern
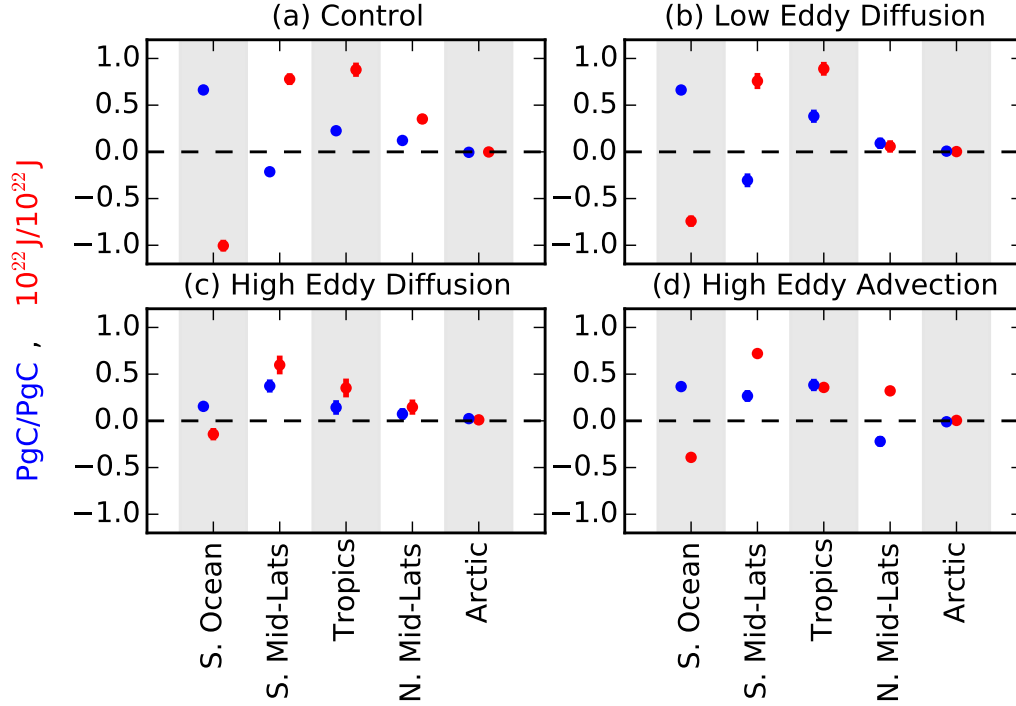
FIGURE 3.7: Linear regression of each region's carbon content against global carbon content (blue) and each regions heat content against global heat content (red). Linear regression 95% confidence interval is shown, but too small to be discerned.

mid-latitudes and tropics (Figure 3.7 (b)). However, the *high mixing* simulations are less clear. The regional heat content is dominated by the southern mid-latitudes with weak compensation between the Southern Ocean and tropics (Figure 3.7 (c) and (d)).

The linear regression of regional carbon content (Figure 3.7, blue dots), however, suggests that the Southern Ocean carbon content variability contributes most towards the global carbon content variability for all simulations. For the *low mixing simulations*, there appears to be a compensation between the southern mid-latitude and tropical carbon content variability. This compensation in regional variability is not seen in the *high mixing simulations* where the regression coefficients are both positive for these two regions. Regardless of these differences, the Southern Ocean is the region with the largest regression coefficient for all simulations.

The time-series of the regional variability for heat and carbon content compared to
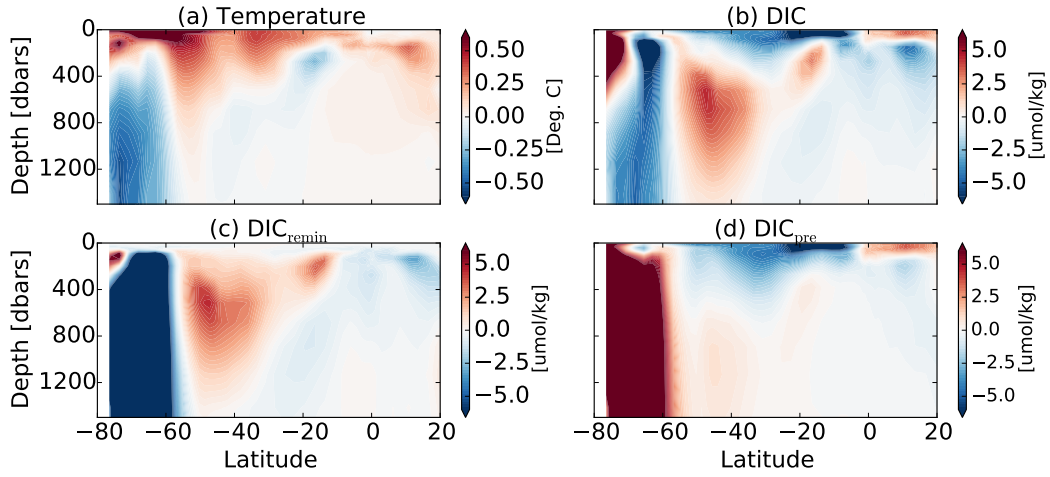
Figure 3.8: Subsurface (a) potential temperature, (b) DIC, (c) remineralized DIC, and (d) preformed DIC for convective year composite from control simulation. Only the surface ocean is shown to highlight the strongest-magnitude features.

the global heat and carbon content are shown in the supplemental information as an additional way to visualize the offsetting variations in different regions.

This relationship between WS deep convection and Southern Hemisphere surface warming is consistent with *Bernardello et al.* [2014] and *Cabre et al.* [2017]. Both papers use the same GFDL model shown here in the control configuration to assess the impact of convection on the climate system and both sets of analysis show similar Southern Hemisphere surface warming in response to a convective event. Specifically, *Cabre et al.* [2017] show that during these winter time convective events, substantial warming occurs in the Southern Ocean, increasing sea surface temperatures, decreasing sea ice and low clouds, and increasing solar radiation absorption. The result is a substantial warming of the Southern Hemisphere surface ocean and atmosphere. This atmospheric warming propagates to the rest of the atmosphere almost instantaneously, changing the meridional temperature gradient and altering the strength of the Hadley Cell in both hemispheres. For a more detailed look at the teleconnections between the Southern Ocean convection and tropical SST increases, we refer the reader to *Cabre et al.* [2017].

3.4 Mechanisms Driving Variability

In order to understand why global heat and carbon content are anti-correlated we look more in depth at the mechanisms driving the regional variability of these quantities.

3.4.1 Heat Content Variability

We first examine the variability of heat content. As shown for the *control* simulation sub-surface temperature in Figure 3.8 (a), convection acts to deplete the Southern Ocean of subsurface heat, and increase the surface heat content in the southern mid-latitudes and tropics. These processes are more explicitly shown in Figure 3.9. Periods of convection (highlighted in grey) are consistent with deepening of the mixed layer (black line), a depletion of subsurface Southern Ocean temperature (green line), an increase in Southern Ocean heat flux into the atmosphere (negative out of ocean – red line), and an increase in southern mid-latitude and tropical SST (blue line). These processes are consistent in the *low eddy diffusion* simulation which also oscillates between convective and non-convective periods (not shown).

This relationship between WS deep convection and Southern Hemisphere surface warming is consistent with *Bernardello et al.* [2014] and *Cabre et al.* [2017]. Both papers use the same GFDL model shown here to assess the impact of convection on the climate system and both sets of analysis show similar Southern Hemisphere surface warming in response to a convective event. Specifically, *Cabre et al.* [2017] show that during these winter time convective events, substantial warming occurs in the Southern Ocean, increasing sea surface temperatures, decreasing sea ice and low clouds, and increasing solar radiation absorption. The result is a substantial warming of the Southern Hemisphere surface ocean and atmosphere. This atmospheric warming propagates to the rest of the atmosphere almost instantaneously, changing the meridional temperature gradient and altering the strength of the Hadley Cell in both hemispheres. For a more detailed look at the telecon-

Figure 3.9: Top: Weddell Sea subsurface temperature as in Figure 3.4 (green) and Weddell Sea mixed layer depth (black). Bottom: Southern Ocean surface heat flux where positive indicates into the ocean (red), Southern Hemisphere SST averaged between 0°–55°S (blue) for the control simulation.

nections between the Southern Ocean convection and tropical SST increases, we refer the reader to *Cabre et al.* [2017].

In this paper we show that the impact of this surface warming in the southern mid-latitudes and tropics is strong enough to counteract the depletion of subsurface heat in the Southern Ocean, resulting in a global increase in heat content after WS convection.

3.4.2 Carbon Content Variability

Next we examine the regional mechanisms driving variability in carbon content in order to understand the anti-correlation between global heat and carbon content. Examining the *control* simulation (Figure 3.8 (b)), we see that during convection there is a strong subsurface depletion of DIC in the Southern Ocean, an increase in subsurface DIC in the southern mid-latitudes, and a further depletion of surface-layer DIC in the southern mid-latitudes to equator. To understand these spatial patterns, we break the DIC up into two

components:

$$DIC = DIC_{pre} + DIC_{remin} \tag{3.4}$$

where the preformed component (DIC_{pre}) is the DIC concentration of the water at the ocean surface and the remineralized component (DIC_{remin}) is the carbon concentration due to biological accumulation. DIC_{pre} is set equal to DIC in the mixed layer and is advected and mixed into the ocean interior with biological sources and sinks set to zero. Thus by definition, DIC_{remin} is zero within the mixed layer and represents the component of DIC in the interior that is due to biological sources and sinks.

When breaking the DIC down into its two components, we see that in the Southern Ocean there is a very strong depletion of subsurface remineralized carbon and a strong increase in preformed carbon (Figure 3.8 (c) and (d)). This signal is consistent with deep convective mixing. The increase in subsurface DIC_{pre} occurs from mixing relatively high surface DIC_{pre} down into the subsurface and the decrease in DIC_{remin} occurs from mixing relatively high DIC_{remin} from the subsurface to the surface layer. Mixing these high DIC waters from the abyssal Southern Ocean to the surface results in outgassing of CO_2 to the atmosphere (not shown) and the net result is a reduction in subsurface DIC.

The depletion in surface DIC in the Southern Hemisphere tropical region on the other hand is entirely due to a depletion in preformed DIC. This region also experiences a strong warming thus reducing the solubility of CO_2 within the surface waters and limiting the amount of DIC that can be held by the water in equilibrium with the atmosphere and at constant alkalinity. To verify that the reduction in solubility is driving the subsequent decrease in DIC, we show the DIC content versus heat content for the tropical region in Figure 3.10 (a). The strong negative relationship supports the hypothesis that the variability in preformed DIC in this region is driven by changes in solubility. Figure 3.10 (a) additionally shows the theoretical change in carbon content given a change in heat content due to solubility alone (constant pCO_2 and alkalinity – black line) with a slope of
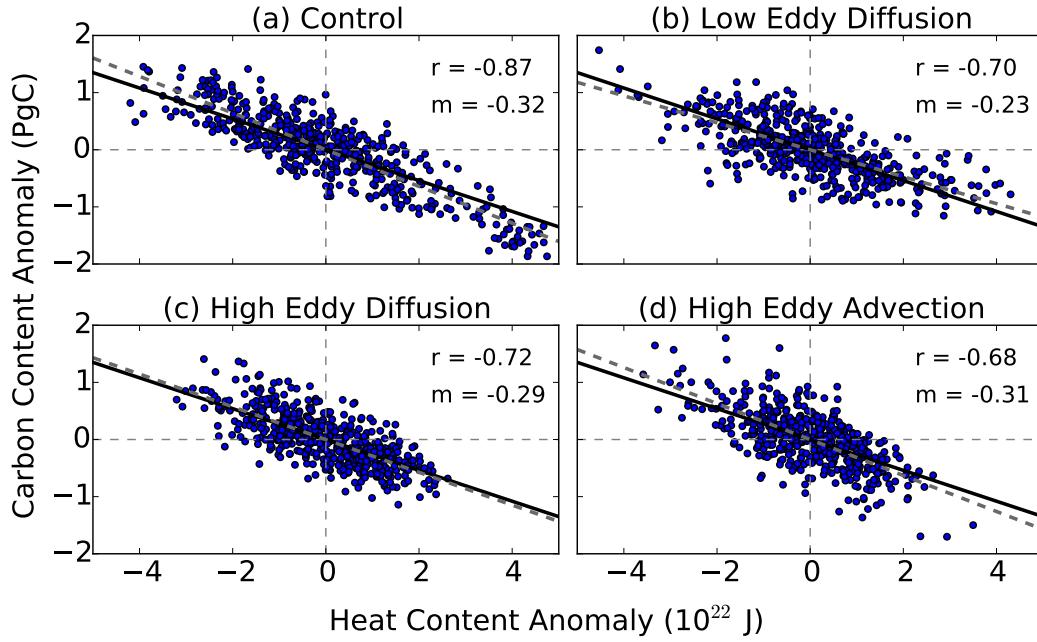
Figure 3.10: Scatter of heat content anomaly vs preformed DIC integrated over the tropical region for each simulation. Dashed grey linear line represents the linear fit of the carbon vs heat data with slope, m, and pearson correlation coefficient r. Solid black linear line represents the projected change in carbon content given a change in heat content with constant alkalinity and pCO_2 in equilibrium with the preindustrial atmosphere (scaled from *Gruber et al.* [1996]).

-0.27 PgC/10^{22}J. This relationship is calculated using the relationship derived in *Gruber et al.* [1996] and scaled to relate carbon content with heat content. There is good agreement between this theoretical model and the linear regression of carbon content versus heat content for this region, represented by the dashed grey line (linear slope values, m, also shown on Figure 3.10), further supporting the hypothesis that carbon variability is consistent with variability in solubility.

The above solubility mechanism appears to hold in all simulations (Figure 3.10 (b) – (d)). All simulations have the same negative relationship between preformed carbon content and heat content integrated over the tropical region (20°S – 20°N) with good agreement with the scaled solubility line (black line). This result suggests that the variability in DIC in this region is driven by variability in the temperature-driven solubility, regardless of the high-latitude convective variability.

Finally we examine the southern mid-latitude subsurface increase in DIC seen in Fig-

ure 3.8 (b). Looking at the components of DIC, it is apparent that this increase is entirely due to remineralized DIC. To understand why this increase of remineralized DIC occurs, we correlate the remineralized DIC anomaly with ideal age in the southern mid-latitude subsurface region (averaged between 40°– 50°S and 200–1000 m, Figure 3.11). The ideal age is a tracer in the model simulation which quantifies the mean time since the water last had contact with the surface. The tracer is set to zero in the mixed layer and ages at a rate of 1 yr yr^{-1} after it leaves the mixed layer. In all simulations, the remineralized DIC anomaly in this region is strongly correlated with ideal age with Pearson correlation coefficients exceeding 0.8 (Figure 3.11). Calculating the linear regression coefficient (m) between the remineralized DIC and ideal age yields a rate of accumulation of remineralized DIC of approximately 0.25 μmol kg^{-1} yr^{-1} for all simulations (Figure 3.11). Comparing this rate of accumulation of remineralized DIC to the modeled local remineralization rate ($jPO_4 \times 108 = 1.6$ μmol kg^{-1} yr^{-1}) we find that the rate of accumulation of remineralized DIC in this region is significantly less than the remineralization rate. The DIC found at a given point has accumulated along many trajectories, some largely passing through surface waters where the local remineralization rate is large, and some passing through deep waters where the local remineralization rate is small. The low slope of the relationship between DIC$_{remin}$ and age suggests that it is changes in the fraction of waters taking deeper trajectories that is most important in explaining the changes in Figure 3.11.

Because only changes in transport cause the ideal age to change, the strong correlation between the remineralized DIC and ideal age suggest the accumulation of DIC$_{remin}$ is due to a slow down of exchange between the surface and subsurface waters. This conclusion is only valid if the rate of local remineralization is constant, or does not impact the time tendency of DIC in this region. Correlation analysis between the modeled remineralization rate and DIC tendency suggest no significant (or very small) correlation between the two variables (see supplemental material Figure 5) indicating the variability in subsurface DIC$_{remin}$ is indeed due to variability in transport.
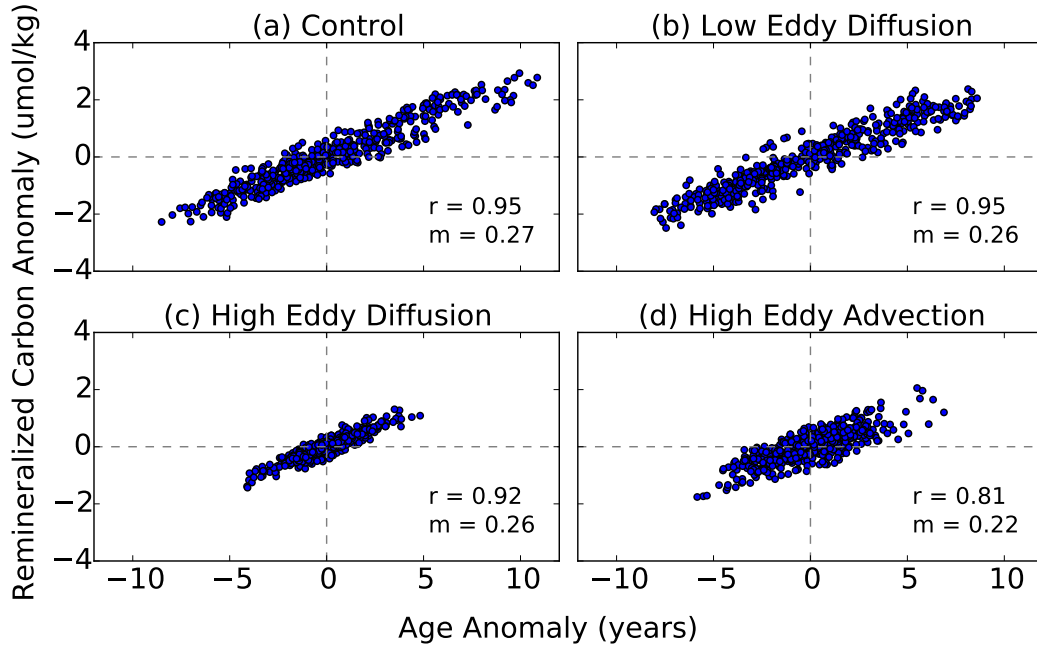
Figure 3.11: Ideal age versus remineralized DIC for all simulations. Quantities are averaged over latitudes 40°–50°S and 200–1000 m. Linear regression coefficients, m, and pearson correlation coefficients, r, are included for reference.

To verify that the same spatial relationship of DIC and its components is consistent in all simulations, we show the covariance of globally integrated DIC against zonally (and vertically) integrated DIC, DIC_{pre}, and DIC_{remin} in Figure 3.12. The general pattern of covariance between the global DIC and remineralized DIC shows a strong positive value in the Southern Ocean followed by a decreasing to negative covariance in the southern mid-latitudes and then increasing again to above zero in the tropics. This pattern is apparent in all simulations, but with different magnitudes due to the different convective variability. When comparing with Figure 3.8 it is important to note that these covariance calculations use the DIC integrated over the entire water column, whereas Figure 3.8 only shows the surface layer (top 1500 dbars). Due to deep spreading of decreased DIC_{remin} values from the Southern Ocean convection into the abyssal mid-latitudes (supplemental Figure S6), the depth-integrated global DIC and remineralized DIC covariance does not become negative until approximately 45°S.

The opposite pattern holds for the covariance between global DIC and preformed
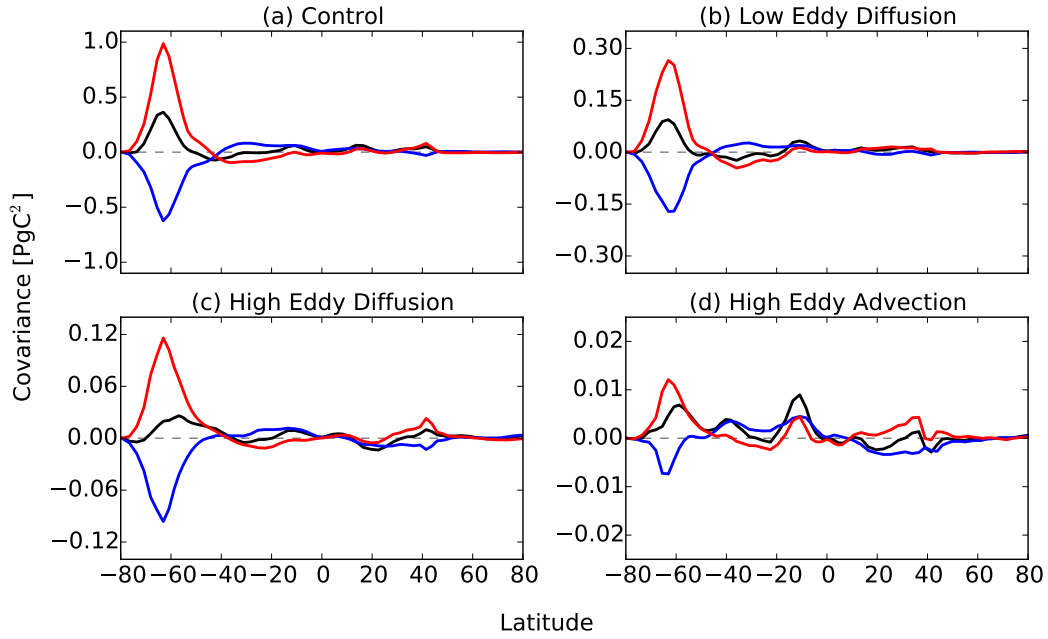
Figure 3.12: Covariance between globally integrated DIC content and DIC (black), preformed DIC (blue) and remineralized DIC (red) for each simulation as a function of latitude. Note different y-axis scales.

DIC: a negative covariance in the Southern Ocean, followed by an increase in covariance in the southern mid-latitudes and a decrease below zero north of the equator. Because of the lack of deep convection in the *high mixing simulations*, the Southern Ocean covariance is significantly smaller than the other simulations (note different y-axis scales in Figure 3.12), but the qualitative relationship remains the same. The consistency in the general shape of these relationships suggests that the same mechanisms are controlling the regional variability in all simulations.

3.5 Conclusions

Using a coupled climate model, we have quantified the global and regional natural variability in oceanic heat and carbon content. We have found that in this model, the highly convective Southern Ocean drives strong global variability in heat and carbon content. Additionally, these two quantities are strongly anti-correlated. Using simulations with different parameter settings for mesoscale mixing, we show that these results are robust

40

across simulations with different WS convective variability, but the anti-correlation relationship is strongest with the two simulations which oscillate between convecting and non-convecting states.

As illustrated in Figure 3.13, the global anti-correlation between heat and carbon content is due to differences in the sign and magnitude of the regional variability. The arrows in the schematic indicate the magnitude of variability and the sign during a convective period. As indicated, the global heat and carbon content are anti-correlated.

In the Southern Ocean, heat and carbon content are both depleted during convection, but the southern mid-latitude and tropical regions each have heat content variability that balance the Southern Ocean variability. The resulting global heat content variability therefore has the same sign and magnitude as the variability in the southern mid-latitudes and tropics. Carbon content variability on the other hand exhibits a cancelation between the southern mid-latitudes and tropics. Therefore, the resulting variability in global carbon content closely follows the variability in the Southern Ocean.

The sub-surface variability structure is also depicted in Figure 3.13 and highlights the differences between heat and carbon. During convection, both quantities decrease in the subsurface Southern Ocean. Additionally, both heat and carbon show increases in the southern mid-latitudes, but the temperature increases are contained in the surface, while DIC increases at depth. This increase in subsurface DIC is likely a result of decreased ventilation. Finally, the southern mid-latitudes and tropics show an increase in surface temperature and a decrease in surface DIC. The variability in DIC here is due to solubility decreases as a result of the temperature increase.

Comparing the magnitude of the modeled natural variability to the size of recent observed trends can provide information on how detectible anthropogenic trends are [*Thomas et al.*, 2015]. For the control simulations, the magnitude of global carbon variability is about ± 3 PgC. This accounts for only approximately 3% of the estimated an-
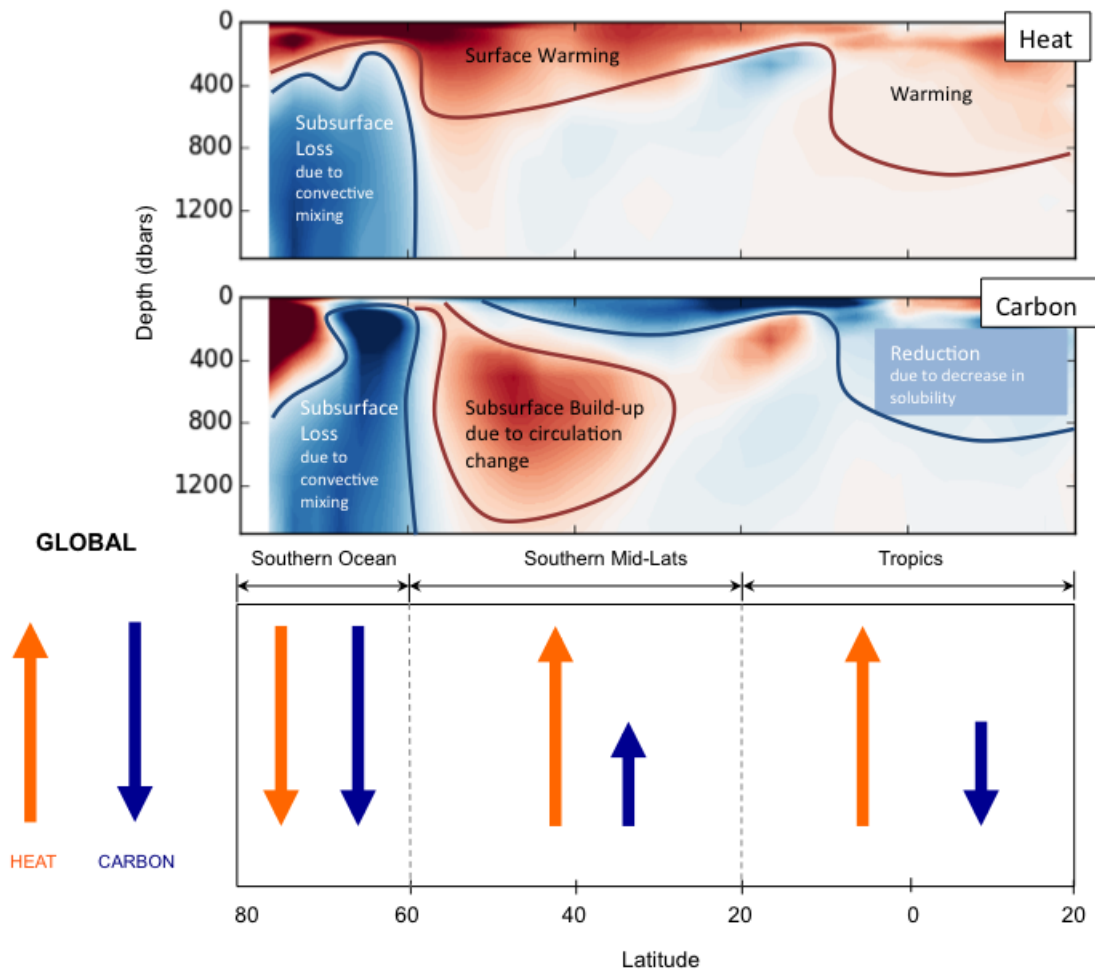
Figure 3.13: Schematic summarizing regional variability in oceanic heat and carbon during a convective year. Arrows designate the sense of global and regional inventory change during a convective year, positive indicating an increase in oceanic content.

thropogenic uptake of carbon over the past few decades [*Khatiwala et al.*, 2012; *Sabine et al.*, 2004; *Waugh et al.*, 2006]. The variability in global heat content on the other hand is about ± 3 ×10^{22} J. This is a much larger percentage (20%) of the estimated uptake of anthropogenic heat in recent decades [*Levitus et al.*, 2009]. These results suggest that changes in carbon content due to anthropogenic activity are unlikely to be obscured by long-timescale variability, but changes in heat content could be obscured. This large natural variability in global heat content could explain why there is less CMIP5 model agreement in oceanic heat uptake than there is for carbon uptake [*Frölicher et al.*, 2009].

If we assume these results hold for the real ocean, we would expect that during the current non-convective period we would experience a subsurface warming in the Southern Ocean and a slowdown of the intermediate water ventilation. Both these processes have been documented in observational studies [*Purkey and Johnson*, 2012; *Waugh et al.*, 2013], but it is important to note that these changes could also be due to anthropogenic influences such as greenhouse gas warming and ozone depletion in addition to variability in WS convection. The frequency of modeled WS convection is a hard to compare to real-life WS convection because of the lack of an observational record in the Southern Ocean. Additionally, *de Lavergne et al.* [2014] have shown that models that have frequent convection in preindustrial control simulations have a significant reduction in convection under global warming scenarios. This suggests that we may not observe another strong WS convective event, and makes it extremely difficult to determine what frequency of WS convection is 'correct'.

The results of this study suggest that the atmosphere could exhibit significant changes in temperature and CO_2 concentration in response to Southern Ocean convective variability. A previous study by *Cabre et al.* [2017] using our control version of the ESM2Mc model shows an increase in SH and global atmospheric temperatures. This is because the additional flux of heat into the ocean is more than balanced (and indeed is driven) by a decrease in clouds and ice, resulting in an additional 0.15 PW of additional shortwave

heating of the Southern Hemisphere when convection is at its peak. An interesting extension of this study would be to examine whether relatively small preindustrial changes in atmospheric carbon dioxide could be associated with changes in SH temperatures, as well as a more comprehensive examination of this process in Earth System Models with variable atmospheric carbon dioxide.

A caveat with this study is that only a single model has been used. More analysis should be conducted with additional model simulations to examine if this relationship and the relative magnitudes of variability between heat and carbon are consistent. Similar analysis with additional models could help to understand the intermodel spread of oceanic carbon content, and the larger intermodel spread in oceanic heat content [*Frölicher et al.*, 2014b], and also provide a better context in which to analyze recent observational trends. Additionally, the model used in this analysis has a relatively coarse resolution and parameterizations for mesoscale eddies. *Dufour et al.* [2017] assessed the impact that model resolution has on WS convection and concluded that horizontal model resolution has an important impact on vertical stratification and the subsurface heat reservoir build-up. However, the impact of resolution is not straightforward - a 1/4 degree ocean behaved more like our high eddy diffusion model with relatively constant convection while a 1/10 degree ocean model showed more stratification and behaved more like our control model. *Griffies et al.* [2015] have additionally examined the impact eddies have on Southern Ocean heat uptake and transport in eddy-permitting models and have concluded that uncertain model parameterizations tend to lead to model drift and less accurate lateral and vertical heat distribution. These impacts need to be kept in mind when discussing model simulations with parameterized eddies.

CHAPTER 4

Relationship between age and oxygen

4.1 Introduction

Understanding ocean circulation is one of the fundamental challenges of physical oceanography. While the large-scale circulation is generally well understood, quantifying smaller scale features is far more challenging. A common tool used in both observational and modeling studies is the concept of water âĂŸageâĂŹ. Quantifying how long since a region of interior water has last has contact with the ocean surface can help in understanding how the water came to be in said location. In modeling studies, an ideal age tracer is often included in ocean model simulations. This ideal age ages at a rate of 1 year per year after the parcel of water has left the mixed layer. In observational studies, quantifying age is far more complicated. A common tool to quantify observational ocean age are transient atmospheric tracers, most often atmospheric CFCsâĂę. While CFCs are a strong tool used to understand ocean circulation, there are some well-documented problems with the methodology. First because of the different time-series of various atmospheric tracers, each tracer will yield a slightly different ocean age than another for the same watermass. Therefore, it can be difficult to reconcile the different ages given by different tracers.

Second, after the Montreal Protocol, and subsequent regulation in CFC emissions, atmospheric concentrations of CFCs have begun to decrease. This turnover in the time-series makes understanding ocean tracer age ambiguous. Finally, the mean age is dependent on the âĂę. One idea that has been suggested is to use oxygen concentration as a proxy for age in the ocean. Oxygen is often time saturation (?) when in the surface mixed layer, and decreases due to biological consumption as it moves through the ocean interior. Gnanadesikan et al., 2012 show a robust relationship between the simulated change in age and change in oxygen in response to a global warming forcing (Gnanadesikan et al, 2012 âĂŞ figure 3)âĂę. In this paper we aim to investigate the relationship between oxygen and age along observational Line W.

4.2 Methods

4.2.1 Observational Data

4.2.2 Mean Age Calculation

4.2.3 Model Data

4.3 Observational Line W

The climatologies of the calculated mean tracer age and oxygen concentration from the observational Line W are shown in Figure 2. The data has been interpolated to a grid with a vertical resolution of XXX and horizontal resolution of XXX. Additionally, the figure shows the average depths of the neutral density surfaces, represented by the black contour lines. Observing the two sub-plots, in general there appears to be a negative relationship between the two. There is relatively increased oxygen concentration, and zero age at the surface. This is consistent with the water being in contact at the surface where the oxygen and CFCs are at near-equilibrium with the atmosphere. Age then generally increases with depth, reaching a local-maxima at just below the average depth of the 27.5 neutral density surface. Oxygen on the other hand generally decreases with depth, reach-

ing a local-minima along the average depth of the 27.5 neutral density surface. While the age and oxygen generally appear to follow a negative relationship, there are hints of a breakdown between this relationship in Figure 2. For example, oxygen increases with depth after the minimum at neutral density surface 27.5, while age also increases (maybe not the best example since this region doesnâĂŹt really show up in the correlation figureâĂę).

In order to further investigate the relationship between mean age and oxygen, the Pearson correlation coefficient between age and oxygen is calculated along Line W and is shown in Figure 3 (a). The figure largely shows the anticipated negative correlation between age and oxygen, however two regions of positive correlation are apparent. One positive correlation region is at approximate depths 500-750 dbars (between neutral density surfaces 27.0 and 27.5), and the second is slightly deeper at depths 1250 âĂŞ 2000 dbars. Given the anticipated anti-correlation relationship between age and oxygen, especially in the ventilated thermocline, these regions of positive correlation are surprising. We additionally examine the relationship between the age and apparent oxygen utilization (AOU): where O_{2sat} is the equilibrium saturation concentration of oxygen, calculated as a function of temperature and salinity, and O_2 is the observed oxygen concentration. The AOU is a measure of how undersaturated the oxygen concentration is. This undersaturation is usually due to biological consumption of oxygen. Analyzing the relationship between AOU and age gives us similar information to the age-oxygen relationship, however, because we are subtracting the oxygen concentration from the oxygen saturation, the AOU-age relationship will be the opposite sign (mainly positive) and the AOU-age relationship ignores the impacts of temperature (and salinity) on oxygen saturation.

The Pearson correlation coefficient between age and AOU is shown in Figure 3 (b). As expected, most of the domain expresses a positive relationship between the two quantities. Similar to the age-oxygen pattern seen in the age-oxygen correlation coefficients (Figure 3 (a)), there are two regions with anomalous correlation. One upper region of zero correla-

tion, consistent with the upper region of positive correlation seen in Figure 3 (a), and one deeper region of negative correlation, consistent with the deep region of positive correlation in Figure 3 (a). The fact that these patterns exist in the age-AOU correlation pattern in addition to the age-oxygen correlation pattern suggest that the signal is not entirely due to temperature influences on oxygen concentration. However it is important to note that the upper region of positive correlation seen in the age-oxygen relationship is significantly reduced in the age-AOU relationship, suggesting some influence of temperature (possibly also show the age-o2 sat correlation? . . . also thinking about maybe changing the sign on AOU to make correlations the same sign).

To better visualize and analyze the relationship between the mean age and oxygen along observational Line W, we show the scatter plot of age versus oxygen in Figure 4 (a). The scatter points are colored with each locationâĂŹs correlation coefficient (same as in Figure 3 (a)). The S-shape of the age-oxygen relationship roughly follows the depth of the water column, with the surface waters at the left end of the S-shape and the deep waters at the right end. The positive correlation regions indicated from Figure 3 (a) also appear in this relationship shown in Figure 4 (a).

Also work on the age-AOU scatter plot.

Age/O2/AOU profilesâĂę

Paragraph with hypothesis for why we get anomalous correlation along like W. Segway into using model for analysis.

4.4   Model Line W

Because of the limited temporal and spatial resolution of the observational data, we additionally examine the age-oxygen relationship in an Earth System Model, GFDL ESM2Mc. The climatology of the ideal age tracer and oxygen concentration along Line W is shown in Figure 6. The modeled oxygen climatology is elevated at the surface and decreases

with depth, with a local-minima between the 26.5 and 27.0 average neutral density surfaces. The oxygen climatology then increases with depth. The modeled age climatology on the other hand is zero at the surface (consistent with the definition of ideal age). The age then increases with depth, with a local-maxima on the 27.0 average neutral density surface. This overall picture is consistent with the observational data (Figure 2), although there is a more obvious offset between the depths of the local oxygen minima and local age maxima. Like with the observational data, this suggests a possible breakdown of the anticipated negative relationship between age and oxygen in this region. To quantify the modeled age-oxygen relationship on Line W we show the Pearson correlation coefficient for the model simulation (Figure 7 (a)). There is a region of positive correlation (with correlation coefficient of approximately 0.4) around depth 500 dbars, starting at distance 400 km and extending to the end of Line W. This region of positive correlation is similar to the upper region of positive correlation seen in the observational record (Figure 3 (a)). Interestingly, in the model simulation, there is no deeper region of positive correlation as seen in the observational correlation. We additionally show the Pearson correlation coefficient for age versus AOU (Figure 7 (b)) in order to remove the impacts of temperature of solubility. The area of anomalous correlation (now negative) around depth 500 dbars is greatly reduced in Figure 7 (b), suggesting that a fraction of the positive correlation seen in the age-oxygen correlation is due to solubility. However, this region still has a reduced positive correlation, suggesting some mechanism is impacting the age-AOU relationship. Similar to the analysis of the observational data, we show the scatter plots of age versus oxygen and AOU in Figure 8âĂę Similar shape to observational data. Positive correlation occurs in the bend, near the oxygen minimum. The shape of the relationship roughly follows depth (approximate depths are indicated on the figure). The figure suggests that the positive correlation could be due to vertical motion acting on the gradients in age and oxygen. Circle back to hypothesis for why we get positive correlation region - segway into further analysis on mechanisms.

4.5 Mechanisms driving positive correlation

Based on the preliminary analysis from both the observational and model data on the age-oxygen relationship, we hypothesize that the positive relationship is due to a significant vertical isopycnal heave coinciding with a same-sign vertical gradient in age and oxygen (in this case a positive vertical gradient). In this section we will investigate this hypothesis further. In order to determine the effects of isopycnal heave on the age-oxygen correlation, we calculate the temporal correlation over the entire North Atlantic basin both on the average depth of various neutral density surfaces:

$$r_{withheave} = corr()$$

and on the time-varying neutral density surfaces:

$$r_{noheave} = corr()$$

In both equations (2) and (3) above, γ_n designates a neutral density surface and the over bar designates the time average. It is important to note that the correlation of age and oxygen on the average depth of a neutral density surface (Equation 2) includes the influences of isopycnal heave. The calculation of the correlation between age and oxygen on the time-varying neutral density surfaces (Equation 3) does not include the impacts of isopycnal heave. Both of these correlations calculated on various neutral density surfaces are shown in Figure 11.

4.6 Conclusions

Bibliography

Arblaster, J. M., and G. A. Meehl (2006), Contributions of External Forcings to Southern Annular Mode Trends, *19*, 2896–2905.

Banks, H. T., and J. M. Gregory (2006), Mechanisms of ocean heat uptake in a coupled climate model and the implications for tracer based predictions of ocean heat uptake, *Geophysical Research Letters*, *33*(7), 3–6, doi:10.1029/2005GL025352.

Bernardello, R., I. Marinov, J. B. Palter, E. D. Galbraith, and J. L. Sarmiento (2014), Impact of Weddell Sea deep convection on natural and anthropogenic carbon in a climate model, *Geophysical Research Letters*, *41*(20), 7262–7269, doi:10.1002/2014GL061313.

Boyer, T. P., C. Stephens, J. I. Antonov, M. E. Conkright, L. A. Locarnini, T. D. O'Brien, and H. E. Garcia (2002), World Ocean Atlas 2001, *Temperature*, *Salinity*, *2*, NOAA Atlas NESDIS 49, 165 pp, doi:http://doi.org/10.7289/V5NZ85MT.

Cabre, A., I. Marinov, and A. Gnanadesikan (2017), Global atmospheric teleconnections and multi-decadal climate oscillations driven by Southern Ocean convection, *Journal of Climate*, *30*, 8107–8126, doi:10.1175/JCLI-D-16-0741.1.

Carsey, F. D. (1980), Microwave Observation of the Weddell Polynya, *Monthly Weather Review*, *108*, 2031–2044.

de Lavergne, C., J. B. Palter, E. D. Galbraith, R. Bernardello, and I. Marinov (2014), Cessation of deep convection in the open Southern Ocean under anthropogenic climate change, *Nature Climate Change*, *4*(4), 278–282.

Dee, D. P., S. M. Uppala, A. J. Simmons, P. Berrisford, P. Poli, S. Kobayashi, U. Andrae, M. A. Balmaseda, G. Balsamo, P. Bauer, P. Bechtold, A. C. M. Beljaars, L. van de Berg, J. Bidlot, N. Bormann, C. Delsol, R. Dragani, M. Fuentes, A. J. Geer, L. Haimberger, S. B. Healy, H. Hersbach, E. V. Hólm, L. Isaksen, P. Kållberg, M. Köhler, M. Matricardi, A. P. McNally, B. M. Monge Sanz, J. J. Morcrette, B. K. Park, C. Peubey, P. de Rosnay,

C. Tavolato, J. N. Thépaut, and F. Vitart (2011), The ERA - Interim reanalysis: configuration and performance of the data assimilation system, *Quarterly Journal of the Royal Meteorological Society*, *137*(656), 553–597.

Devries, T., M. Holzer, and F. Primeau (2017), Recent increase in oceanic carbon uptake driven by weaker upper-ocean overturning, *Nature Publishing Group*, *542*(7640), 215–218, doi:10.1038/nature21068.

Dufour, C. O., A. K. Morrison, S. M. Griffies, I. Frenger, H. Zanowski, and M. Winton (2017), Preconditioning of the Weddell Sea polynya by the ocean mesoscale and dense water overflows, *Journal of Climate*, pp. JCLI–D–16–0586.1, doi:10.1175/JCLI-D-16-0586.1.

Dunne, J. P., J. G. John, A. J. Adcroft, S. M. Griffies, R. W. Hallberg, E. Shevliakova, R. J. Stouffer, W. Cooke, K. A. Dunne, M. J. Harrison, J. P. Krasting, S. L. Malyshev, P. C. D. Milly, P. J. Phillipps, L. T. Sentman, B. L. Samuels, M. J. Spelman, M. Winton, A. T. Wittenberg, and N. Zadeh (2012), GFDL's ESM2 Global Coupled ClimateâĂŞCarbon Earth System Models. Part I: Physical Formulation and Baseline Simulation Characteristics, *Journal of Climate*, *25*(19), 2247–2267.

Fan, T., C. Deser, and D. P. Schneider (2014), Recent Antarctic sea ice trends in the contect of Southern Ocean surface climate variations since 1950, *Geophysical Research Letters*, pp. 1–8.

Fetterer, F., K. Knowles, W. Meier, M. Savoie, and A. K. Windnagel. (2016), updated daily, *Sea Ice Index*, *Version 2*, pp. Boulder, Colorado USA. NSIDC: National Snow and Ic, doi: http://dx.doi.org/10.7265/N5736NV7.

Frölicher, T. L., F. Joos, G. K. Plattner, M. Steinacher, and S. C. Doney (2009), Natural variability and anthropogenic trends in oceanic oxygen in a coupled carbon cycle-climate model ensemble, *Global Biogeochemical Cycles*, *23*(1), doi:10.1029/2008GB003316.

Frölicher, T. L., J. L. Sarmiento, D. J. Paynter, J. P. Dunne, J. P. Krasting, and M. Winton (2014a), Dominance of the Southern Ocean in Anthropogenic Carbon and Heat Uptake in CMIP5 Models, *Journal of Climate*, *28*(2), 862–886.

Frölicher, T. L., M. Winton, and J. L. Sarmiento (2014b), Continued global warming after CO2 emissions stoppage, *Nature Climate Change*, *4*(1), 40–44.

Galbraith, E. D., A. Gnanadesikan, J. P. Dunne, and M. R. Hiscock (2010), Regional impacts of iron-light colimitation in a global biogeochemical model, *Biogeosciences*, *7*, 1043–1064, doi:10.5194/bgd-6-7517-2009.

Galbraith, E. D., E. Y. Kwon, A. Gnanadesikan, K. B. Rodgers, S. M. Griffies, D. Bianchi, J. L. Sarmiento, J. P. Dunne, J. Simeon, R. D. Slater, A. T. Wittenberg, and I. M. Held (2011), Climate Variability and Radiocarbon in the CM2Mc Earth System Model, *Journal of Climate*, *24*(16), 4230–4254.

Galbraith, E. D., J. P. Dunne, A. Gnanadesikan, R. D. Slater, J. L. Sarmiento, C. O. Dufour, G. F. de Souza, D. Bianchi, M. Claret, K. B. Rodgers, and S. S. Marvasti (2015), Compled functionality with minimal computation: Promise and pitfalls of reduced-tracer ocean biogeochemistry models, *Journal of Advances in Modeling Earth Systems*, *7*, 2012–2028, doi:10.1002/2015MS000463.

Gent, P. R., and J. C. Mcwilliams (2010), Isopycnal Mixing in Ocean Circulation Models, *Journal of Physical Oceanography*, *20*(1), 150–155.

Gent, P. R., J. Willebrand, T. J. McDougall, and J. C. Mcwilliams (1995), Parameterizing Eddy-Induced Tracer Transports in Ocean Circulation Models, *dx.doi.org*, *25*(4), 463–474.

Gillett, N. P. (2005), Detection of external influence on sea level pressure with a multi-model ensemble, *Geophysical Research Letters*, *32*(19), L19,714–4.

Gillett, N. P., and D. W. J. Thompson (2003), Simulation of recent Southern Hemisphere climate change, *Science*, *302*(5643), 273–275.

Gillett, N. P., F. W. Zwiers, A. J. Weaver, and P. A. Stott (2003), Detection of human influence on sea-level pressure, *Nature*, *422*(6929), 292–294.

Gillett, N. P., J. C. Fyfe, and D. E. Parker (2013), Attribution of observed sea level pressure trends to greenhouse gas, aerosol, and ozone changes, *Geophysical Research Letters*, *40*(10), 2302–2306.

Gnanadesikan, A. (1999), A Simple Predictive Model for the Structure of the Oceanic Pycnocline, *283*, 2077–2079.

Gnanadesikan, A., M.-A. Pradal, and R. P. Abernathey (2015), Isopycnal mixing by mesoscale eddies significantly impacts oceanic anthropogenic carbon uptake, *Geophysical Research Letters*, *42*(11), 4249–4255, doi:10.1002/2015GL064100.

Gong, D., and S. Wang (1999), Definition of Antarctic Oscillation index, *Geophysical Research Letters*, *26*(4), 459–462.

Gordon, A. L. (1982), Weddell Deep Water variability, *Journal of Marine Research*, *40*, 199–217.

Griffies, S. M., M. Winton, W. G. Anderson, R. Benson, T. L. Delworth, C. O. Dufour, J. P. Dunne, P. Goddard, A. K. Morrison, A. Rosati, A. T. Wittenberg, J. Yin, and R. Zhang (2015), Impacts on Ocean Heat from Transient Mesoscale Eddies in a Hierarchy of Climate Models, *Journal of Climate*, *28*, 952–977, doi:10.1175/JCLI-D-14-00353.1.

Gruber, N., J. Sarmiento, and T. Stocker (1996), An improved method for detecting anthropogenic CO2 in the oceans, *Global Biogeochemical Cycles*, *10*(4), 809–837, doi:doi:10.1029/96GB01608.

Hall, A., and M. Visbeck (2002), Synchronous Variability in the Southern Hemisphere Atmosphere, Sea Ice, and Ocean Resulting from the Annular Mode, *Journal of Climate*, pp. 1–15.

Kalnay, E., M. Kanamitsu, R. Kistler, W. Collins, D. Deaven, L. Gandin, M. Iredell, S. Saha, G. White, J. Woollen, Y. Zhu, M. Chelliah, W. Ebisuzaki, W. Higgins, J. Janowiak, K. C. Mo, C. Ropelewski, J. Wang, A. Leetmaa, R. Reynolds, R. Jenne, and D. Joseph (1996), The NCEP/NCAR 40-year reanalysis project, *Bulletin of the American Meteorological Society*, *77*(3), 437–471.

Kanamitsu, M., W. Ebisuzaki, J. Woollen, S.-K. Yang, J. J. Hnilo, M. Fiorino, and G. L. Potter (2010), NCEPâĂŞDOE AMIP-II Reanalysis (R-2), *Bulletin of the American Meteorological Society*, *83*(11), 1631–1643.

Khatiwala, S., F. Primeau, and T. Hall (2009), Reconstruction of the history of anthropogenic CO(2) concentrations in the ocean., *Nature*, *462*(7271), 346–9, doi:10.1038/nature08526.

Khatiwala, S., F. Primeau, and M. Holzer (2012), Ventilation of the deep ocean constrained with tracer observations and implications for radiocarbon estimates of ideal mean age, *Earth and Planetary Science Letters*, *325-326*, 116–125.

Kobayashi, S., Y. Ota, and Y. Hatada (), The JRA-55 Reanalysis : General Specifications and Basic Characteristics.

Landschutzer, P., N. Gruber, F. A. Haumann, R. Christian, D. C. E. Bakker, S. V. Heuven, M. Hoppema, N. Metzl, C. Sweeney, and T. Takahashi (2015), The Reinvigoration of the Southern Ocean Carbon Sink, *Science*, *349*(6253), 1221–1224, doi:10.1126/science.aab2620.

Latif, M., T. Martin, and W. Park (2013), Southern Ocean Sector Centennial Climate Variability and Recent Decadal Trends, *Journal of Climate*, *26*(19), 7767–7782.

Le Quere, C., J. C. Orr, P. Monfray, and O. Aumont (2000), Interannual variability of the oceanic sink of CO2 from 1979 through 1997, *Global Biogeochemical Cycles*, *14*(4), 1247–1265.

Lee, S., and S. B. Feldstein (2013), Detecting Ozone- and Greenhouse GasâĂŞDriven Wind Trends with Observational Data, *Science*, *339*(6119), 563–567.

Lenton, A., F. Codron, L. Bopp, N. Metzl, P. Cadule, A. Tagliabue, and J. L. Sommer (2009), Stratospheric ozone depletion reduces ocean carbon uptake and enhances ocean acidification, *Geophysical Research Letters*, *36*, 1–5, doi:10.1029/2009GL038227.

Levitus, S., J. I. Antonov, T. P. Boyer, R. A. Locarnini, H. E. Garcia, and A. V. Mishonov (2009), Global ocean heat content 1955-2008 in light of recently revealed instrumentation problems, *Geophysical Research Letters*, *36*(7), 1–5, doi:10.1029/2008GL037155.

Lovenduski, N. S., N. Gruber, S. C. Doney, and I. D. Lima (2007), Enhanced CO2 out-gassing in the Southern Ocean from a positive phase of the Southern Annular Mode, *Global Biogeochemical Cycles*, *21*(2), doi:10.1029/2006GB002900.

Marinov, I., A. Gnanadesikan, J. L. Sarmiento, J. R. Toggweiler, M. Follows, and B. K. Mignone (2008), Impact of oceanic circulation on biological carbon storage in the ocean and atmospheric pCO2, *Global Biogeochemical Cycles*, *22*(3), n/a–n/a.

Marshall, G. J. (2003), Trends in the Southern Annular Mode from Observations and Re-analyses, *Journal of Climate*, *16*(24), 4134–4143.

Martinson, D. G., P. D. Killworth, and A. L. Gordon (1981), A Convective Model for the Weddell Polynya, *Journal of Physical Oceanography*, *11*, 466–488.

Mignone, B. K., A. Gnanadesikan, J. L. Sarmiento, and R. D. Slater (2006), Central role of Southern Hemisphere winds and eddies in modulating the oceanic uptake of anthropogenic carbon, *Geophysical Research Letters*, *33*(1), L01,604.

Ollitrault, M., and A. Colin de Verdière (2002), SOFAR Floats Reveal Midlatitude Intermediate North Atlantic General Circulation. Part I: A Lagrangian Descriptive View, *Journal of Physical Oceanography*, *32*(7), 2020–2033.

Parkinson, C. L., and D. J. Cavalieri (2012), Antarctic sea ice variability and trends, 1979-2010, *The Cryosphere*, *6*(4), 871–880.

Polvani, L. M., and K. L. Smith (2013), Can natural variability explain observed Antarctic sea ice trends? New modeling evidence from CMIP5, *Geophysical Research Letters*, *40*(12), 3195–3199.

Pradal, M.-A., and A. Gnanadesikan (2014), How does the Redi parameter for mesoscale mixing impact global climate in an Earth System Model?, *Journal of Advances in Modeling Earth Systems*, *6*(3), 586–601, doi:10.1002/2013MS000273.

Previdi, M., and L. M. Polvani (2014), Climate system response to stratospheric ozone depletion and recovery, *Quarterly Journal of the Royal Meteorological Society*, *140*(685), 2401–2419.

Purkey, S. G., and G. C. Johnson (2012), Global contraction of Antarctic Bottom Water between the 1980s and 2000s, *Journal of Climate*, *25*(17), 5830–5844, doi:10.1175/JCLI-D-11-00612.1.

Redi, M. H. (1982), Oceanic Isopycnal Mixing by Coordinate Rotation, *Journal of Physical Oceanography*, *12*, 1154–1158.

Roemmich, D., J. Gilson, R. Davis, P. Sutton, S. Wijffels, and S. Riser (2007), Decadal Spinup of the South Pacific Subtropical Gyre, *Journal of Physical Oceanography*, *37*(2), 162–173.

Russell, A. M., and A. Gnanadesikan (2014), Understanding multidecadal variability in ENSO amplitude, *Journal of Climate*, *27*(11), 4037–4051, doi:10.1175/JCLI-D-13-00147. 1.

Sabine, C. L., R. A. Feely, N. Gruber, R. M. Key, L. Kitack, J. L. Bullister, R. Wanninkhof, C. S. Wong, D. W. R. Wallace, B. Tillbrook, F. J. Millero, T.-H. Peng, A. Kozyr, T. Ono, and A. F. Rios (2004), The Oceanic Sink for Anthropogenic CO, *Science, 305*, 367–371.

Sarmiento, J. L., and C. Le Quere (1996), Oceanic Carbon Dioxide Uptake in a Model, *Science*, *274*, 1346–1350.

Sarmiento, J. L., and J. R. Toggweiler (1984), A new model for the role of the oceans in determining atmospheric pCO 2, *Nature*.

Sen Gupta, A., and M. H. England (2006), Coupled OceanâĂŞAtmosphereâĂŞIce Response to Variations in the Southern Annular Mode, *Journal of Climate*, *19*(18), 4457–4486.

Seviour, W. J. M., A. Gnanadesikan, D. W. Waugh, and M.-A. Pradal (2017), Transient response of the Southern Ocean to changing ozone: Regional responses and physical mechanisms, *Journal of Climate*, pp. JCLI–D–16–0474.1, doi:10.1175/JCLI-D-16-0474. 1.

Swart, N. C., and J. C. Fyfe (2012), Observed and simulated changes in the Southern Hemisphere surface westerly wind-stress, *Geophysical Research Letters*, *39*(16), L16,711.

Thomas, J. L., D. W. Waugh, and A. Gnanadesikan (2015), Southern Hemisphere extratropical circulation: Recent trends and natural variability, *Geophysical Research Letters*, *42*(13), 5508–5515.

Thompson, D. W. J. (2002), Interpretation of Recent Southern Hemisphere Climate Change, *Science*, *296*(5569), 895–899.

Thompson, D. W. J., J. M. Wallace, and G. C. Hegerl (2000), Annular Modes in the Extratropical Circulation. Part II: Trends, *Journal of Climate*, *13*, 1018–1036.

Thompson, D. W. J., S. Solomon, P. J. Kushner, M. H. England, K. M. Grise, and D. J. Karoly (2011), Signatures of the Antarctic ozone hole in Southern Hemisphere surface climate change, *Nature Publishing Group*, *4*(11), 741–749.

Visbeck, M. (2009), A Station-Based Southern Annular Mode Index from 1884 to 2005, *Journal of Climate*, *22*(4), 940–950.

Waugh, D. W., T. M. Hall, B. I. McNeil, R. Key, and R. J. Matear (2006), Anthropogenic CO2 in the oceans estimated using transit time distributions, *Tellus B*, *58*(5), 376–389.

Waugh, D. W., F. Primeau, T. DeVries, and M. Holzer (2013), Recent Changes in the Ventilation of the Southern Oceans, *Science*, *339*(6119), 568–570.

Winton, M., S. M. Griffies, B. L. Samuels, J. L. Sarmiento, and T. L. Frölicher (2013), Connecting Changing Ocean Circulation with Changing Climate, *Journal of Climate*, *26*(7), 2268–2278.

Xie, P., and G. K. Vallis (2012), The passive and active nature of ocean heat uptake in idealized climate change experiments, *Climate Dynamics*, *38*(3-4), 667–684, doi: 10.1007/s00382-011-1063-8.

Jordan Thomas

Born: May 4, 1990
Wichita, KS

Education

Johns Hopkins University (August 2012 – Present)   Baltimore, MD
    PhD in Earth and Planetary Science
    Masters in Earth and Planetary Science
    Dissertation: Investigating Natural Variability in the Climate System
Pennsylvania State University (August 2008– May 2012)   University Park, PA
    Bachelors of Science in Meteorology
    Concentration in Atmospheric Sciences
University of Southampton (January 2011 – July 2011)   Southampton, UK
    Minor in Oceanography

Publications

Thomas J. L., Waugh D. W., and Gnanadesikan A. (2017) "Relationship between ocean heat and carbon variability". *Journal of Climate*. Submitted

Brune W. H., Baier B. C., Thomas J.L., Ren X., Cohen R. C., Pusede S. E., Browne E. C., Goldstein A. H., Gentner D. R., Keutsch F. N., Thornton J.A., Harrold S., Lopez-Hilfiker F. D. and Wennbergm P. O. (2016) "Ozone production chemistry in the presence of urban plumes". *Faraday Discussions*. 189. 169–189.

Thomas J. L., Waugh D. W., and Gnanadesikan A. (2015) "Southern Hemisphere extra-tropical circulation: Recent trends and natural variability". *Geophysical Research Letters*. 42. 5508–5515.

Pusede S. E., Gentner D. R., Wooldridge P. J., Browne E. C., Rollins A. W., Min K.-E., Russell A. R., Thomas J. L., Zhang L., Brune W. H., Henry S. B., DiGangi J. P., Keutsch F. N., Harrold S. A., Thornton J. A., Beaver M. R., St. Clair J. M., Wennberg P. O., Sanders J., Ren X., VandenBoer T. C., Markovic M. Z., Guha A., Weber R., Goldstein A. H., and Cohen R. C. (2014) "On the temperature dependence of organic reactivity, nitrogen oxides, ozone production, and the impact of emission controls in San Joaquin Valley, California". *Atmospheric Chemistry and Physics*. 14. 3373–3395.

Experience

Johns Hopkins University | RESEARCH ASSISTANT
September 2012 – Present

- Researched the impact of ozone depletion on atmospheric and oceanic circulation biogeochemistry.

- Performed statistical analysis on output from 27 coupled climate model simulations (CMIP5) using Python to determine that recent trends in atmospheric quantities are likely caused by anthropogenic activities.

- Designed and executed model simulations using a fully coupled General Circulation Model to investigate relationship between ocean heat and carbon content.

- Analyzed model output using post-processing techniques in Python and MATLAB, focusing on atmosphere-ocean interactions, ocean dynamics, ocean biogeochemistry and ocean acidification.

- Presented dissertation research at multiple scientific conferences and invited talks including at University of Pennsylvania and MIT.

Johns Hopkins University | TEACHING ASSISTANT
September 2015 – December 2015

- Developed and taught interactive lessons focused on global and environmental change.

- Facilitated bi-weekly review sessions and held weekly office hours to assist with questions and homework.

Pennsylvania State University | UNDERGRADUATE RESEARCH ASSISTANT
August 2009 – May 2012

- One of two students selected from Penn State to participate in CalNEX 2010, an air quality research campaign in Bakersfield, CA.

- Studied oxidation photochemistry and preformed analysis and model comparison with collected data.

- Developed an instrument to measure in-situ tropospheric ozone production.

- Analyzed air-quality data to diagnose large scale meteorological patters.